JGR Atmospheres

RESEARCH ARTICLE

10.1029/2025JD044937

Statistical Models for Infrasonic Propagation: Application to the Detection Capability of the Global IMS Network

A. Le Pichon[1], P. Hupe[2], J. Vergoz[1], S. Kristoffersen[1], C. Listowski[1], E. Marchetti[3], D. Gheri[3], and L. Ceranna[2]

[1]CEA, DAM, DIF, Arpajon, France, [2]BGR, Hannover, Germany, [3]Department of Earth Sciences, University of Florence, Florence, Italy

Key Points:

- A realistic statistical framework is proposed to quantify the detection probability of the International Monitoring System (IMS) network for atmospheric explosions
- The 1 kt design goal of the IMS network to detect any atmospheric explosion is achieved at any time of the year with 53 certified IMS stations
- Detection threshold variations can reach one order of magnitude from seasonal down to semi-diurnal scales

Supporting Information:

Supporting Information may be found in the online version of this article.

Correspondence to:

A. Le Pichon,
alexis.le-pichon@cea.fr

Citation:

Le Pichon, A., Hupe, P., Vergoz, J., Kristoffersen, S., Listowski, C., Marchetti, E., et al. (2025). Statistical models for infrasonic propagation: Application to the detection capability of the global IMS network. *Journal of Geophysical Research: Atmospheres*, *130*, e2025JD044937. https://doi.org/10.1029/2025JD044937

Received 22 JUL 2025
Accepted 15 NOV 2025

Author Contributions:

Conceptualization: A. Le Pichon, L. Ceranna
Data curation: A. Le Pichon, P. Hupe, J. Vergoz
Formal analysis: A. Le Pichon, P. Hupe, J. Vergoz, S. Kristoffersen, C. Listowski
Investigation: A. Le Pichon, P. Hupe, J. Vergoz, S. Kristoffersen, C. Listowski
Methodology: A. Le Pichon, P. Hupe, J. Vergoz, S. Kristoffersen, L. Ceranna
Supervision: A. Le Pichon
Validation: A. Le Pichon, P. Hupe, S. Kristoffersen, C. Listowski, E. Marchetti, D. Gheri

Abstract

The detection capability of the global infrasound International Monitoring System (IMS) deployed to monitor compliance with the Comprehensive Nuclear-Test-Ban Treaty is highly variable in space and time. Previous studies estimated the source energy of near-surface explosions from remote observations using empirical yield-scaling relations. However, these relations simplify the complexities of infrasound propagation. In order to reduce the variance in the predicted wave attenuation, massive numerical propagation simulations are carried out by exploring a wide range of realistic atmospheric scenarios. An analytical expression is proposed to model transmission losses at distances up to 4,000 km. This attenuation relation is validated using multi-year near- and far-field records of volcanic eruptions from Mount Etna, Italy, as a benchmark. An idealized explosive source model is combined with transmission loss and measured noise statistics to quantify the 90% probability detection threshold of the IMS network. This approach yields high-resolution detection capability simulation results with limited computational resources. Simulations predict that explosions equivalent to ∼500 t of TNT equivalent would be detected by at least two stations at any time of the year, with the detection capability being best during the solstice periods. Due to the high spatio-temporal variability of the winds in the ground-to-stratosphere levels, threshold variations can reach one order of magnitude from seasonal down to semi-diurnal scales.

Plain Language Summary

The global infrasound International Monitoring System (IMS) has been designed to monitor compliance with the Comprehensive Nuclear-Test-Ban Treaty. Its detection capability varies greatly in both space and time. Previous research oversimplifies the complexities involved in infrasound propagation when estimating the energy from near-surface explosions. To minimize the errors in the predicted wave attenuation, extensive numerical propagation simulations are conducted, examining a broad range of realistic atmospheric conditions. An analytical formula is introduced to model transmission losses over distances of up to 4,000 km. This attenuation model is validated against multi-year records of volcanic eruptions from Mount Etna, Italy, serving as a benchmark. An idealized explosive source model is integrated with transmission loss and measured noise statistics to determine the detection threshold of the IMS network. This method provides high-resolution simulation results while using limited computational resources. The simulations indicate that explosions equivalent to ∼500 t of TNT would be detected by at least two stations at any time throughout the year, with the detection capability peaking during solstice periods. Due to the significant variability of winds from ground to stratosphere levels, threshold variations can differ by an order of magnitude from seasonal to semi-diurnal scales.

1. Introduction

Interest in infrasound technology and research was revived after the Comprehensive Nuclear-Test-Ban Treaty (CTBT) was adopted and opened for signature in 1996. The infrasound component of the International Monitoring System (IMS) is being deployed and will comprise 60 infrasound stations homogeneously distributed across the globe (Christie & Campus, 2009). The primary function of the IMS infrasound stations is to monitor compliance with the CTBT (CTBTO, 2019). The IMS network has been designed with the objective of reliably detecting and locating an atmospheric nuclear explosion with a minimum yield of 1 kiloton (kt) of TNT equivalent, at any time and point on the globe. As of July 2025, 53 of these stations have been certified and are sending data in near real-time to the International Data Center, which is located in Vienna, Austria (Mialle et al., 2018).

Visualization: A. Le Pichon, P. Hupe, J. Vergoz
Writing – original draft: A. Le Pichon, P. Hupe, S. Kristoffersen
Writing – review & editing: A. Le Pichon, P. Hupe, J. Vergoz, S. Kristoffersen, C. Listowski, E. Marchetti, D. Gheri, L. Ceranna

Each infrasound station is an array of microbarometers that are sensitive to acoustic pressure variations in the frequency band to detect explosions (between 0.02 and 4 Hz). The array configurations generally include 4 to 15 elements, with typical designs comprising 4 to 8 elements, and apertures ranging from 1 to 3 km (Marty, 2018). Despite the fact that the IMS network is not yet fully established, it currently provides global coverage of infrasound sources generating pressure waves, which can propagate over thousands of kilometers with weak attenuation (e.g., Drob et al., 2003; Sutherland & Bass, 2004). In addition to its primary function for monitoring CTBT compliance, this network is capable of locating and characterizing geophysical and anthropogenic events (e.g., Christie & Campus, 2009; Mialle et al., 2018).

Systematic reprocessing of IMS infrasound data emphasizes long lasting detections from permanent sources as well as persistent transient signals. Advanced data products were derived from the reprocessing of 18 years (2003–2020) of continuous records at 53 certified IMS stations (Hupe et al., 2022). The resulting data products encompass globally repeating infrasound sources, including mountain-associated waves (Hupe et al., 2019) characterized by periods ranging from 20 to 50 s, ocean ambient noise (referred to as microbaroms) in the 0.1–0.6 Hz band (De Carlo et al., 2021), or persistently active volcanoes and large explosive eruptions above ∼0.5 Hz (Gheri et al., 2023; Matoza et al., 2018). Local sources such as surf (Arrowsmith & Hedlin, 2005), man-made activities above 1 Hz (Brachet et al., 2009; Campus & Christie, 2009), thunderstorms (Farges et al., 2021) and dam releases (Che et al., 2023) were also highlighted. These products have been identified as useful tools for assessing the relative quality of IMS data (Kristoffersen et al., 2022). They also help advance the development of prototypes for early warning systems (e.g., Marchetti et al., 2018), and contribute to refine knowledge on the dynamics of the middle atmosphere (MA, from ∼12–90 km) where data coverage is sparse (e.g., Letournel et al., 2024).

Methodologies incorporating various yield-scaling relationships have been proposed to assess the capability of the IMS network (e.g., Clauter & Blandford, 1997; Stevens et al., 2002). Significant advances have been achieved using the Los Alamos National Laboratory (LANL) yield-amplitude scaling relation derived from recordings of historical atmospheric nuclear and chemical explosions. Building on the LANL yield-amplitude relation (Whitaker, 1997; Whitaker et al., 2003) and the US Air Force Technical Applications Center (AFTAC) yield-period scaling relations (Edwards et al., 2006), Green and Bowers (2010) developed a probabilistic model to calculate the detection threshold of the IMS network. By incorporating a state-of-the-art climatological model (Drob et al., 2008) and a mean uniform station noise amplitude of 0.02 Pa (Bowman et al., 2009), simulations predict that nuclear explosions of ∼400 t of TNT equivalent would be detected by two stations with a 90% probability over 95% of the Earth's surface.

The capacity of the IMS infrasound network to detect near-surface atmospheric explosions strongly depends on station-specific environmental noise. Consequently, the characterization of ambient infrasound noise, encompassing both coherent and incoherent phenomena, is crucial for quantifying the recording environment at each station. Le Pichon et al. (2009) conducted deterministic simulations using the LANL relation, realistic specifications of the stratospheric wind dynamics and site/time/frequency-dependent noise models. Network performance simulations predict a yearly averaged detection threshold of ∼500 t. The large seasonal variation (from ∼50 t to ∼1 kt) indicates the importance of an accurate description of the stratospheric wind dynamics. These studies highlighted the dominant effect of the general circulation of the stratosphere on the IMS network performance, which controls to a first order whether the signal from an explosion is detectable above the noise level at the receivers.

However, the conclusions derived from the LANL yield-amplitude scaling relation may be misleading, as the complexities of atmospheric structure are oversimplified and the used relation does not adequately describe long-range infrasound propagation. Analyses of well-calibrated reference events have revealed a significant spread in yield estimates, which has been attributed to either substantial variability in along-path stratospheric wind speed (Green et al., 2011), or systematic overestimates of a known yield (Fee et al., 2013).

Le Pichon et al. (2012) developed an empirical attenuation relation (referred to as LP12) derived from numerous parabolic equation simulations using synthetic 1D atmospheric velocity models. This relationship is frequency dependent and strongly depends on the effective sound speed parameter (C_{eff}), which is calculated as the sum of the adiabatic sound speed and the wind speed in the horizontal direction of propagation, averaged in the stratopause region. It predicts the transmission loss of the dominant infrasonic arrival (either stratospheric or thermospheric) at a given distance. This relation has been adopted in numerous studies to explain trends in global and multi-station observations (e.g., de Groot-Hedlin & Hedlin, 2014; Marchetti et al., 2018; Walker et al., 2013). However, the model is limited in its application by two factors. First, the idealized atmospheric scenarios underestimate the strength of the stratospheric wind jet. Second, the used climatologies in the mesosphere and lower thermosphere (MLT) do not reproduce realistic enough dynamics of the upper atmosphere and miss interannual variability that influence infrasound propagation.

Today, numerical modeling techniques provide a basis for understanding the role of different factors describing the source (Garcés, 2018) and the atmosphere that affect propagation predictions (Waxler & Assink, 2018). Blom et al. (2023) proposed a statistical framework to quantify the infrasound detection capability using an explosive source model, statistical transmission loss and station noise models. The finite-frequency modal propagation method was applied to construct transmission loss statistics from an historical archive of atmospheric specifications. Spatial and seasonal trend analysis was conducted for different locations across the United States to quantify propagation characteristics and related monitoring capability of above-ground explosions. This approach provides a valuable tool for source characterization at a regional scale. It also reduces yield estimate uncertainties (Blom et al., 2018; Marcillo et al., 2013; Morton & Arrowsmith, 2014) when compared with generic propagation models used for operational processing (Mialle et al., 2018).

The primary objective of the present study is to develop a physical and frequency-dependent attenuation relation that accounts for a realistic description of the spatio-temporal variability of the MA. Atmospheric states are extracted at all IMS stations from historical archives of numerical weather prediction (NWP) model products. Empirical orthogonal function (EOF) analysis is then applied to reduce the ensemble of atmospheric samples into a smaller representative data set of reasonable size to conduct a propagation simulation campaign. Since unresolved small-scale atmospheric perturbations play an important role in returning acoustic energy to the ground (e.g., Drob et al., 2013; Kulichkov, 2009), 2D fields of horizontal wind velocity fluctuations induced by naturally occurring gravity waves (GWs) are incorporated in the original atmospheric profiles.

In the first part, the sampled atmospheric structures are utilized as input into full-wave numerical propagation simulations. For a realistic description of station noise statistics, power spectral densities (PSDs) were computed for continuous records of the 53 certified IMS stations on an hourly basis over a 4-year period.

In the second part, an analytical attenuation relation is derived by applying a multi-dimensional curve-fitting approach to the simulation ensemble. We develop a statistical approach that combines a spectral model of surface explosions with transmission loss and measured noise statistics.

In the result section, the statistical transmission loss model is validated using multi-year records of volcanic eruptions from Mount Etna, Italy, as a benchmark. The detection threshold of the global IMS infrasound network is estimated over a 3-year period with an hourly time resolution.

We then discuss the implications of the proposed approach, which, compared to previous studies, provides progress toward more realistic and more accurate space- and time-dependent detection levels with reliable confidence intervals.

2. Data

2.1. Sampling the Earth's Atmosphere

The dynamic and poorly sampled nature of the middle and upper atmosphere poses a significant challenge to the representation of infrasound propagation with a suitable spatial resolution. To address this challenge, researchers have employed the HWM/MSIS climatological models (Drob, 2018; Drob et al., 2003; Picone et al., 2000) in numerous studies for examining the detection capability (Green & Bowers, 2010; Le Pichon et al., 2009). These models include detailed parameterizations of seasonal changes of the stratosphere and MLT dynamics, providing time-dependent temperature and composition profiles, as well as zonal and meridional wind estimates.

Below ~50 km altitude, NWP models provide a global coverage of the Earth's atmosphere for more realistic atmospheric waveguide predictions (e.g., Ceranna et al., 2009). Above that height and despite having their top around 80 km altitude, NWP operational models get relatively more biased (e.g., Le Pichon et al., 2015) due to poor observational constraints available for data assimilation systems, and because of the numerical damping (sponge layer) used to ensure numerical stability. We use the Whole Atmosphere Community Climate Model

(WACCM) forecast products issued by the National Center for Atmospheric Research (Atmospheric Chemistry Observations & Modeling, National Center for Atmospheric Research, University Corporation for Atmospheric Research, 2020). Atmospheric fields are simulated using WACCM version 6 (Gettelman et al., 2019). Model top is around 135 km and horizontal resolution is 0.9° × 1.25° with 88 vertical levels. WACCM runs are initialized and nudged by the NASA Goddard Earth Observing System model (Rienecker et al., 2008), Version 5, using zonal (U) and meridional (V) winds and temperature. WACCM provides a more realistic description of dynamical processes in the MLT region compared to climatology and a more physical treatment of the upper layers compared to operational NWP products. This database along with WACCM-X, which is related to the WACCM ionospheric extension (Gasperini, 2019), have been successfully employed to describe large-scale geometric waveguides through numerical propagation modeling (e.g., Letournel et al., 2024; Vorobeva et al., 2023).

Vertical profiles of zonal and meridional wind and temperature are extracted at the locations of the 53 IMS stations on the 15th of each month in 2022. Each day is sampled with a temporal resolution of six hours, allowing the representation of the dynamics of the MA, including atmospheric tide oscillations that affect propagation paths in the MLT region (Assink et al., 2012). The direction of propagation within an atmospheric slice greatly alters the transmission loss at the ground. Propagation scenarios are augmented by changing the sign of the projected zonal and meridional winds (from upwind to downwind scenario, or vice-versa); subsequently, propagation conditions in the west, east, north, and south directions are considered. Overall, the ensemble of archived atmospheric specifications comprises 10,176 2D atmospheric fields (53 stations × 12 days × 4 hr × 4 directions).

2.2. Building an Ensemble of Atmospheric Scenarios

We construct a representative ensemble of atmospheric scenarios as an input for propagation modeling without requiring computationally expensive simulation campaigns. The original atmospheric data is reduced via a singular value decomposition. Previous studies found that 10 to 12 empirical orthogonal functions (EOF) can accurately reproduce wind structures in the stratosphere and MLT (Assink et al., 2013). In this study, 10 basis functions are used to construct atmospheric samples that capture 95% of the wind variance (Figure 1b).

Propagation simulations show that tropospheric ducting may occur up to distances of ∼750 km, characteristic of the scale size of tropospheric weather disturbances (Drob et al., 2003). Over horizontal propagation paths of several thousands of kilometers, atmospheric conditions are no longer favorable for persistent tropospheric propagation. Considering that stratospheric waveguides control to first order the detection capability, the whole suite of atmospheric scenarios is divided in different classes of atmospheric regimes in the stratopause region. The stratospheric waveguide is represented by the effective sound speed ratio (C_{eff_r}), a dimensionless parameter that serves as a proxy for parameterizing its influence on long-range infrasound propagation. C_{eff_r} is defined as the ratio between the maximum of C_{eff} between 30 and 70 km and the sound speed at the ground level. Twenty-three classes of C_{eff_r} ranging from 0.7 to 1.4 with a step of 0.05 are constructed. To provide a more detailed description of the transition between the downwind and upwind stratospheric propagation regimes, C_{eff_r} is sampled with a finer grid between 0.9 and 1.1 (Le Pichon et al., 2012).

The statistical independence of the EOFs allows for the construction of a subset of the atmospheric state ensemble considering covariance conditions between the coefficients. The variability of the original atmospheric scenarios is covered by the kernel density estimate regardless the IMS stations and time considered (Blom et al., 2023). For each class of C_{eff_r}, a reduced set of 100 atmospheric states is generated by sampling EOF coefficient values (Figure 2). Above this number, the mean and variance of C_{eff_r} converge to constant values.

One of the main problems in infrasonic propagation is the uncertainty due to unresolved dynamical processes in the MA. Operational atmospheric models are usually unable to explicitly simulate realistic amplitudes of gravity waves (GWs) originating from various sources such as orography, convection, wind shear, jets, and fronts (Lott & Millet, 2009). GWs relevant to infrasound propagation prediction have horizontal scales of hundreds of kilometers and vertical scales of a few kilometers, while time scales range from 5 min to tens of hours. They significantly affect infrasound propagation in the stratopause region, where ray-turning heights are quite sensitive to small-scale atmospheric perturbations (e.g., Chunchuzov et al., 2011; Cugnet et al., 2018).

Green et al. (2011) investigated the influence of an empirical model of GWs to explain explosion detections by diffraction and scattering of acoustic energy in the geometric shadow zone. Hedlin and Drob (2014) showed the influence of unresolved subgrid-scale atmospheric structures to adequately explain the observed wave signal

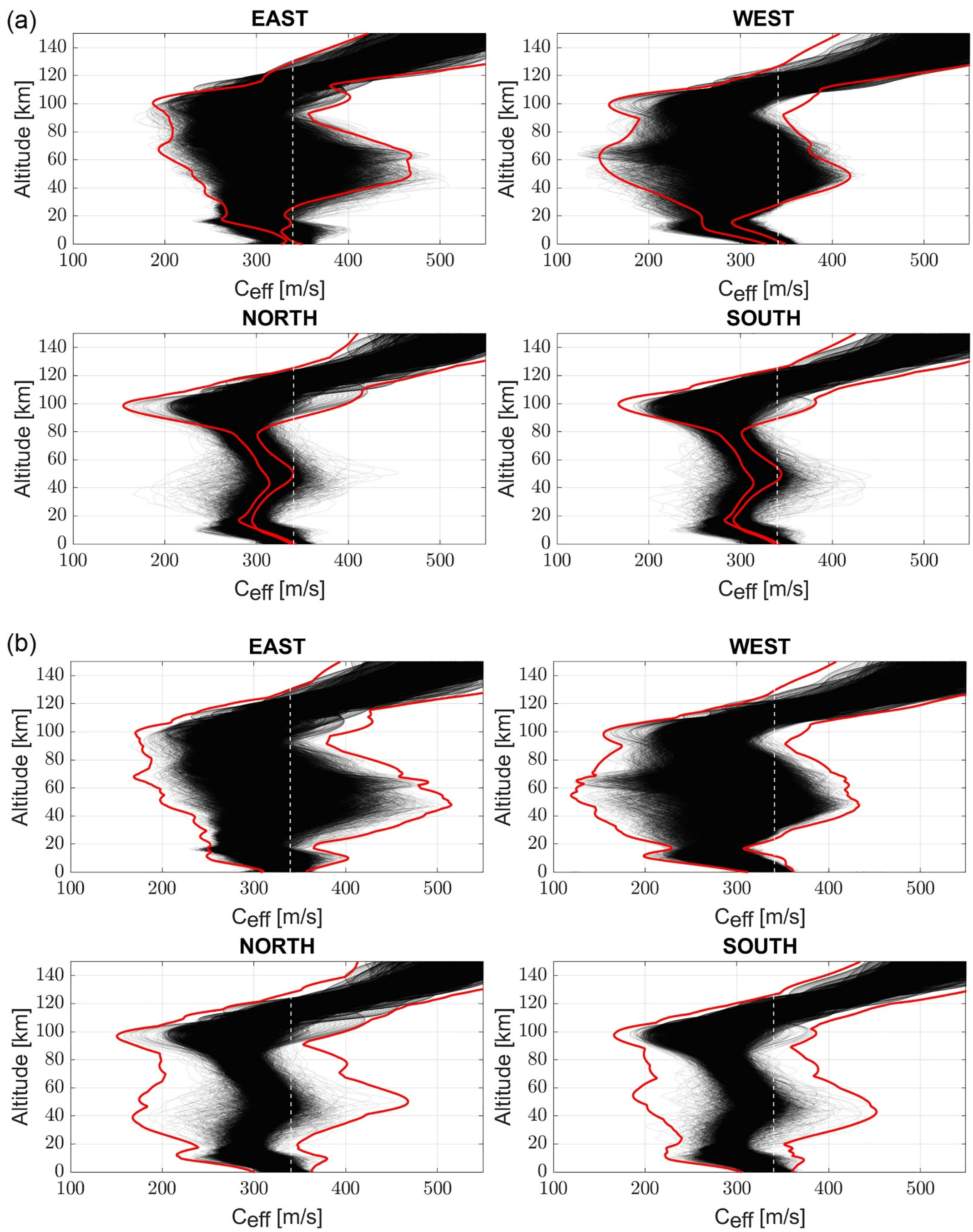

Figure 1. Empirical orthogonal function analysis applied to the 10,176 atmospheric scenarios using (a) 3 and (b) 10 basis functions for eastward/westward (top rows) and northward/southward (bottom rows) propagation directions. The red curves delimit the envelopes of the reconstructed vertical profiles.

duration. Other studies provide methods to represent a 3D stochastic and time-dependent GW field model that is self-consistent with the atmospheric mean flow and suitable for infrasound propagation calculations (e.g., Drob et al., 2013). Further evaluations have been conducted by Listowski et al. (2024) to quantify the impact of GWs on predicting transmission losses across the IMS.

Small-scale wind perturbations are generated using the spectral model of Gardner et al. (1993). This model provides height-dependent horizontal wind perturbation amplitude spectra that compare favorably with meteorological observations at scales between tens and thousands of kilometers. Its spectrum is independent of time and

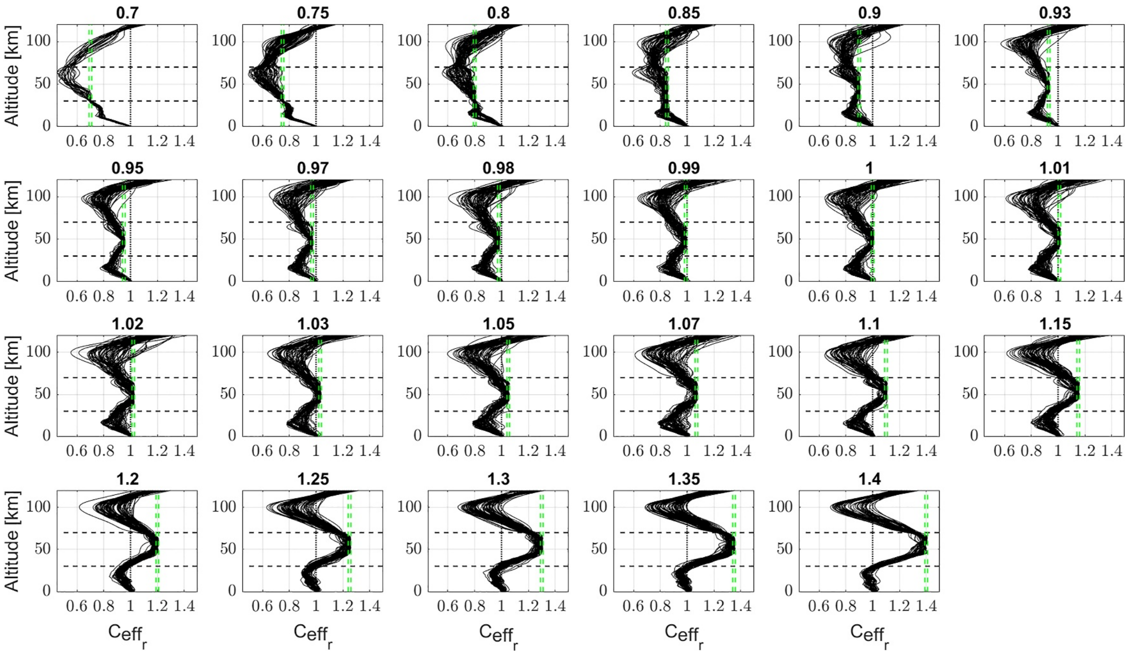

Figure 2. Reduced ensemble of atmospheric states profiles divided into 23 classes of C_{eff_r} containing 100 samples each. The dashed vertical green lines indicate the maximum of $C_{eff_r} \pm 0.01$ between 30 and 70 km.

geographic position and is considered as a tractable global average. Since the Gardner model predicts only wave amplitude spectra, a random phase Fourier inversion of the spectra is performed to generate realizations of horizontal wind perturbation profiles for the simulations. The influence of the perturbations on the modeling is examined by running a series of random-phase inverted models. Gaussian weighting functions are used to combine the vertical profiles to generate 2D wind perturbation fields. The range-dependent variability accounts for the horizontal correlation length of GWs as described by Gardner et al. (1993). GW profiles are added to each member of the reduced ensemble of WACCM effective sound speed profiles. Fourty random realizations of GW profiles are used to keep computation costs manageable while still capturing 90% of the wind variance. Finally, 92,000 (23 classes of $C_{eff_r} \times 100$ samples $\times$ 40 GW realizations) 2D effective sound speed profiles are generated from the ground level to an altitude of 130 km, covering a horizontal range of up to 4,000 km, with a horizontal step size of 0.1°.

2.3. Building Reference Transmission Loss Curves

Infrasound propagation can be modeled using classical acoustic geometric ray-tracing. However, this high-frequency approximation method becomes inappropriate when the spatial extent of the atmospheric structures is comparable to the acoustic wavelength. In this context, low-cost numerical methods in the frequency domain have been used extensively. They provide reasonable attenuation accuracy over long propagation distances, as well as insightful modeling results for improved source localization estimates and robust infrasound source characterization (Blom et al., 2018; Green et al., 2011; Marcillo et al., 2013). Thus, infrasound wavefields have been studied at high resolution over a dense regional network (Le Pichon et al., 2021) to global distances (Walker et al., 2013). These numerical methods also contribute to the development of NWP applications by studying the stratospheric propagation of nearly continuous signals with a time resolution ranging from hours to several years (Assink, Le Pichon et al., 2014; Letournel et al., 2024).

We apply the 2D linear wide-angle parabolic equation (2D-PE) method to the reference data set described in the previous section. This technique overcomes several limitations of the ray method, including the validity of the high-frequency approximation by accounting for diffraction effects near shadow zone boundaries and scattering from small atmospheric inhomogeneities. The 2D-PE method operates in the frequency domain and thus approximates solutions to the convective Helmholtz equation in cylindrical coordinates. It implements the split-step Pade numerical scheme, which allows for large spatial and grid spacing (Waxler & Assink, 2018). The chosen

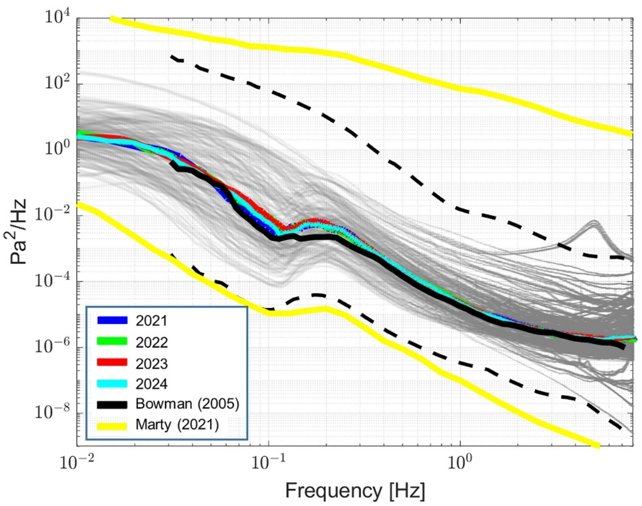

Figure 3. Yearly averaged power spectral densities curves at 53 International Monitoring System (IMS) stations from 2021 to 2024 (gray curves) versus Bowman et al. (2005) and Marty et al. (2021) reference noise models. Median noise distributions of all stations computed for the same year are color coded. The median, 5th and 95th percentiles of the Bowman noise distribution calculated using 21 globally distributed IMS stations are shown by the solid and dashed black lines, respectively. The Marty low and high noise models (1st and 99th percentiles, respectively) calculated using 16 selected IMS stations are shown by the yellow lines.

absorption model includes contributions from both classical (translation and diffusion) and relaxation (rotation and vibration) losses. Frequency-dependent attenuation coefficients are calculated from vertical profiles of temperature, pressure, and concentration of gases up to 160 km altitude (Sutherland & Bass, 2004).

The propagation problem is simplified assuming a flat terrain with infinite ground impedance at sea level. To ensure that sufficient frequency bands capture signals over a wide range of explosive source yields, simulations are performed at the following center frequencies: 0.1, 0.2, 0.4, 0.8, 1.6, and 3.2 Hz (Green & Bowers, 2010), resulting in a total of 552,000 (92,000 × 6) simulations.

2.4. Updating Global Ambient Noise Model

The ability to detect and identify signals of interest is limited by the time-varying station noise level above which signals can be reliably detected (Bowman et al., 2005; Le Pichon et al., 2018; Marty et al., 2021). Above the frequency range of GWs (about $3 \cdot 10^{-3}$ Hz), the incoherent part of the noise fluctuations measured at the infrasound array is mainly produced by wind and eddies (Bowman et al., 2005; Christie & Campus, 2009; Marty et al., 2021). Turbulent eddies generated by wind shear in the boundary layer cause the wind-generated noise amplitude to decrease approximately inversely with frequency (Walker & Hedlin, 2009).

Power spectral densities (PSDs) were computed for continuous records of the 53 certified IMS stations on an hourly basis over a 4-year period (2021–2024). The Welch (1967) technique is applied to a window length of 400 s using a Hanning function with 75% overlap. A total of approximately 19 million PSDs were computed. This systematic processing of background noise allows for an assessment of the sensitivity of each measurement system to geographic and environmental parameters that include both wind-generated noise and coherent signals from geophysical and anthropogenic events.

Figure 3 compares the global median PSD curves at 53 IMS stations for the years 2021–2024 with the median, low and high models (5th and 95th percentiles) calculated by Bowman et al. (2005, 2009). Marty et al. (2021) calculated low and high noise (1st and 99th percentiles) models by removing erroneous and non-calibrated data and deconvolving records from the measurement system responses. The reference curves, displayed in Figure 3, were calculated using data collected at 16 selected IMS stations equipped with field calibration systems, installed at different latitudes and environments. An overall good consistency is found between these models with weak interannual variability.

The ambient noise at infrasound stations is highly variable by season, time of day, and station. The median noise spectra for an individual station may vary by two orders of magnitude in the 0.01–8 Hz band. Geographical and environmental parameters, such as the latitude of the station, local wind conditions, or proximity to the coasts, significantly affect the amplitude of the measured pressure fluctuation (Marty et al., 2021). The type of vegetation surrounding the sensor sites also plays a significant role in reducing the amplitude of wind-generated pressure fluctuations (Raspet & Webster, 2013).

Figure 4 shows examples of seasonal and diurnal PSD variabilities at three IMS stations located at different latitudes. Of the 60 IMS infrasound stations, 23 are located on oceanic islands. While ensuring global network coverage, most of these sites do not offer an ideal environment to ensure good detection capacity, as they are exposed to strong winds and surf noise (Le Pichon et al., 2004). Located on Robinson Crusoe Island, station I14CL (Figure 4a) is permanently exposed to wind, which is the most significant source of infrasonic noise throughout the year and time of day.

The diurnal variation of atmospheric conditions over land caused by surface heating during the day has a significant effect on the wind and temperature distributions, which causes turbulence at the ground surface. The daily variation of the local wind greatly influences the level of infrasound noise. At I19DJ (Djibouti, Figure 4b), the

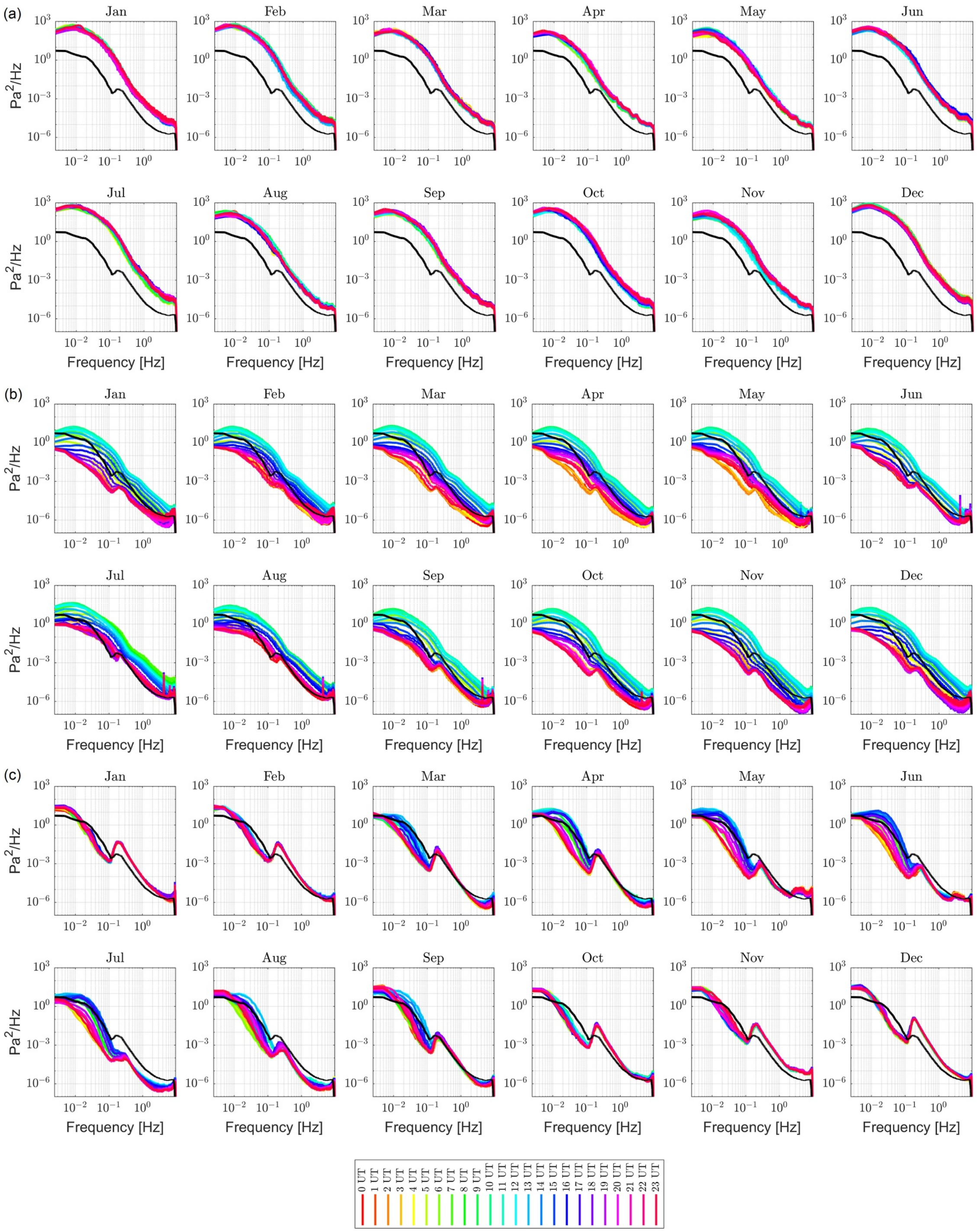

Figure 4. Median hourly power spectral densities curves per month in 2024, color-coded by time of day at (a) I14CL Robinson Crusoe Island (33.8S, 80.7W), (b) I19DJ Djibouti (11.3N, 43.5E), and (c) I37NO Norway (69.5N, 25.5E). The black curve depicts the Bowman et al. (2005) median reference curve. It is noteworthy that these three arrays were not operational at the time analyzed by Bowman et al. (2005).

diurnal variability of PSDs is two orders of magnitude in the 0.02–8 Hz band in all seasons and the amplitude range remains stable over the year. Station-dependent factors that contribute to noise include natural sources, such as microbaroms, which vary smoothly in an annual pattern. At most stations, the dominant microbarom peak is observed during local winter (De Carlo et al., 2021).

10.1029/2025JD044937

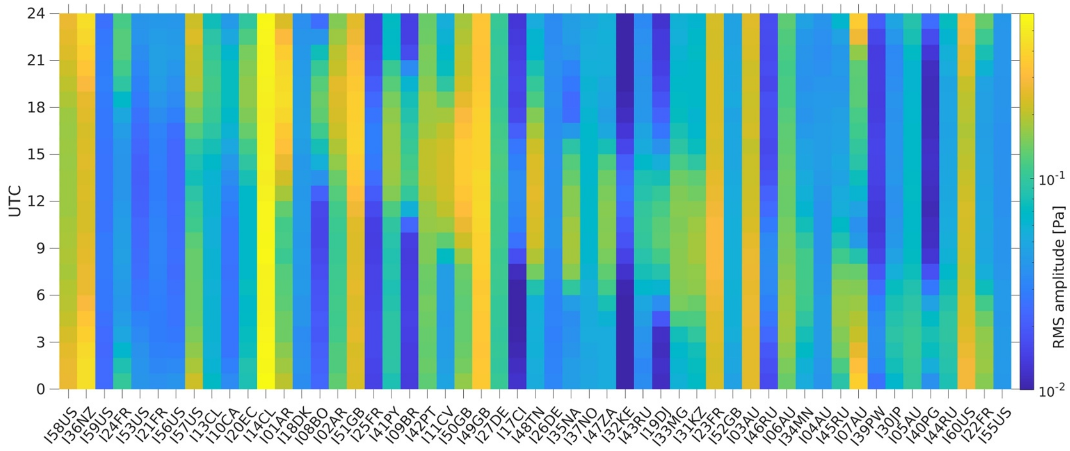

Figure 5. Median hourly RMS amplitudes (2021–2024) at 53 International Monitoring System stations (x-axis, sorted by longitude from west to east) in the 0.1–4 Hz band.

The noise level at station I37NO (Norway, Figure 4c), exhibits a clear seasonal variation in the microbarom peak within three orders of magnitude. As observed for I19DJ in all seasons, diurnal wind noise fluctuations are observed for I37NO from March to September. In winter, the snow cover and lack of solar heating in the atmosphere significantly dampen this fluctuation.

Figure 5 shows the median (2021–2024) of PSD-derived RMS amplitudes for 53 IMS stations per hour of the day (UTC). The stations are sorted by longitude from west to east. A streak of high RMS amplitudes from the upper left to the lower right is noted. As expected, the noise level generally increases with the local daytime, when local wind noise, as well as turbulence and anthropogenic background noise at higher frequencies generally increase. Island stations exhibit high noise amplitudes like I14CL (Robinson Crusoe Island), I23FR (Kerguelen), I42PT (Azores), I49GB (Tristan da Cunha), I51GB (Bermuda), and I58US (Midway), due to their exposed locations to trade winds and surf noise, compared to other continental stations, like I26DE, located in a dense forest far from oceanic sources (e.g., De Carlo et al., 2021).

To calculate the probability distribution of the effective noise at the station, we consider the constraints of evaluating the smallest measurable signal amplitude at the receivers (Blom et al., 2023). This value is controlled by the signal-to-noise ratio (SNR) at which a detection can be confidently made. In the ideal case of perfectly correlated signals and incoherent noise, the SNR improvement from array processing can be related to the square root of the number of array elements N (Green & Bowers, 2010; Mykkeltveit et al., 1983). PSDs are converted to pressure (in Pa) as follows

$$P(f,R,N) = \sqrt{PSD(f)\,\frac{\tau(R)}{N}}, \tag{1}$$

where $\tau(R)$ denotes the wavetrain duration. Green and Nippress (2019) proposed a linear relationship for $\tau(R)$ that increases with range due to the increasing separation between the fastest and slowest arrivals trapped in different waveguides. For waves propagating in waveguides with low along-path variability (range of C_{eff_r} lower than 0.1), $\tau(R) = 0.278R + 122$. When the propagation conditions show waveguide variability (C_{eff_r} range greater than 0.1, which is expected for a propagation range of 4,000 km), $\tau(R)$ reaches a constant value of 305 s for source-to-receiver distances exceeding 3,000 km.

3. Models

3.1. A Physical-Based Attenuation Relation

The amplitude of an infrasonic wave generally tends to decrease with distance from the source. In particular, geometric spreading and dissipation are relevant in determining wave attenuation. In addition, multipath scattering in a heterogeneous medium can significantly affect the observed wave amplitude. To model the infrasound transmission loss, an analogy is made to the seismic attenuation law developed by Pasolini (2008). Assuming that geometrical spreading, reflection and transmission of energy at the interfaces as well as wave interaction effects with small-scale heterogeneities are the main causes of seismic wave attenuation, the amplitude decrease with distance from the source R (in km) is described by

$$A = A_0 \cdot R^{-\frac{n}{2}} \cdot e^{-\gamma R}, \tag{2}$$

where A_0 is the source amplitude, the term $R^{-\frac{n}{2}}$ accounts for geometrical spreading with $n = 2$ for body waves and $n = 1$ for surface waves, and the exponential term γ summarizes the effects of anelastic attenuation and scattering.

We expand Equation 2 to the following expression (denoted LP25), which models geometric spreading in the first shadow zones and wave dissipation that governs attenuation in the far-field:

$$A_p = R^{-\alpha\left(1+\alpha_s\left(1-\cos\left(2\pi\frac{R-R_0}{d_s}\right)\right)\right)e^{-\frac{R-R_0}{R_s}}} \cdot e^{\alpha_g(R-R_0)e^{-\frac{R-R_0}{R_g}}} \cdot e^{-\beta(R-R_0)}, \tag{3}$$

where A_p is the attenuation of the pressure wave at a distance R (in km) from the source, calculated from a reference distance R_0 set to 1 km. Above this reference distance, infrasound can be treated as linear elastic waves rather than non-linear shock waves as the excess pressure is usually small compared to ambient atmospheric pressure (Johnson, 2003). While this assumption holds generally for chemical explosions in the air, it is debatable for large nuclear explosions. According to the blast model by Kinney and Graham (1985, Table XI), the peak amplitude of blast waves for a 1 kt nuclear explosion reaches approximately 8,000 Pa at a distance of 1 km. This amplitude is sufficiently large that it falls outside the scope of linear theory, which may pose a limitation for the proposed source model.

Equation 3 consists of three terms. The first one describes the geometrical spreading in the shadow zone with the parameter α. The wave reflection at the surface is recovered by the cosine function. The dimensionless parameter α and the scaling distance d_s (set to 90 km) control the periodic structure of subsequent stratospheric/thermospheric bounces and the amplitude attenuates exponentially with R. The second term provides a mechanism for acoustic penetration into the first geometrical shadow zones; it allows a correction for the ensonification which is governed by R_g set to 200 km and the parameter α_g (in km^{-1}). The last term controls the wave dissipation through the parameter β (in km^{-1}).

For a given C_{eff_r} and frequency f, the five parameters α, β, α_s, d_s and α_g are calculated by applying a damped non-linear least squares algorithm to the 2D-PE simulation data set (Moré, 1978). The Levenberg-Marquardt algorithm interpolates between the Gauss-Newton algorithm and the gradient descent method. Its robustness allows minimizing problems even when the initial solution is far from the final minimum (Gavin, 2013). Text S1 provides the means and (where applicable) standard deviations of α (Table S1 in Supporting Information S1), β (Table S2 in Supporting Information S1), α_s (Table S3 in Supporting Information S1), α_g (Table S4 in Supporting Information S1) and d_s (Table S5 in Supporting Information S1), which depend on C_{eff_r} and f. From these tabulated values, Equation 3 is used to calculate the mean (μ_{TL}) and standard deviation (σ_{TL}) of the transmission loss for a given distance, frequency and C_{eff_r}.

A realistic distribution is proposed to model transmission loss statistics. Similar multipath transmission loss problems in the context of acoustic (ultrasound) (Tsui et al., 2016; Zhang et al., 2012) and radio communications (Abbas & Sheikh, 1996; Gómez-Déniz & Gómez-Déniz, 2024; Nakagami, 1960) have shown that the Nakagami-m distribution provides a good fit for transmission losses. We therefore use this distribution to model parabolic equation simulations for different classes of C_{eff_r} at all frequencies.

The Nakagami-m distribution is defined as

$$\rho_{arr}(P) = \frac{2m^m}{\Gamma(m)\Omega^m} P^{2m-1} e^{\left(-\frac{m}{\Omega}P^2\right)}, \tag{4}$$

where P is the pressure in Pa, Γ is the Gamma function. The Nakagami-m shape (m) and scale (Ω) parameters are defined by

$$m = \frac{\left(\sigma_{TL}^2 + \mu_{TL}^2\right)^2}{4\mu_{TL}^2\sigma_{TL}^2}, \quad \Omega = \sigma_{TL}^2 + \mu_{TL}^2. \tag{5}$$

The mean (μ_{TL}) and the standard deviation (σ_{TL}) of the transmission loss are determined by

$$\mu_{TL} = \frac{1}{N}\sum_{i=1}^{N} A_{p_i}, \tag{6}$$

$$\sigma_{TL} = \sqrt{\frac{1}{N-1}\sum_{i=1}^{N}\left(A_{p_i}^2 - \mu_{TL}^2\right)}, \tag{7}$$

where A_{p_i} is defined by Equation 3.

Figure 6 compares the predicted pressure attenuation with the Nakagami distribution probability for different source frequencies and typical upwind ($C_{eff_r} < 1$) and downwind ($C_{eff_r} > 1$) scenarios. The shape (m) and scale (Ω) parameters of the Nakagami distribution are defined using the mean, μ, and standard deviation, σ, obtained from the attenuation relation (Equation 3). The attenuation relation explains the simulations in the classical shadow zone and the geometric duct region. Downwind, the stratospheric duct is well established; waves refracted in the stratosphere return to the ground and propagate with weak attenuation (near 60 dB at 4,000 km and 1.6 Hz); the attenuation weakly depends on frequency. This behavior is in contrast to the upwind situation, where waves propagating upward through the MLT are attenuated due to low particle density and non-linear dissipation; this is due to the higher degree of thermo-viscous absorption in the upper atmosphere, which scales quadratically with acoustic frequency (Sutherland & Bass, 2004). At 0.1 Hz, the attenuation reaches ∼80 dB at 3,000 km; above 0.8 Hz, the attenuation exceeds 80 dB at 1,000 km. Overall, the standard deviations of the simulated and fitted transmission losses agree with an average root mean square error of less than 5 dB.

Figure 7 compares the simulated transmission losses with the multi-dimensional curve fitting results at 0.1, 0.8, and 1.6 Hz. The simulated and predicted attenuation values are in good agreement with averaged root mean square errors of 3.2, 4.5 and 6 dB at 0.1, 0.8 and 1.6 Hz, respectively. Above 0.8 Hz, the largest differences exceed 20 dB for upwind propagation ($C_{eff_r} < 0.8$). However, such an error has limited impact as it occurs in a situation where detection is unlikely with attenuation larger than 120 dB. Overall, the attenuation follows an approximately binary variation with C_{eff_r}. This step-like variation is more pronounced at higher frequencies (above 0.8 Hz), while at 0.1 Hz, the attenuation is less sensitive to the strength and direction of the prevailing stratospheric winds. This behavior explains the seasonal patterns in multi-year global infrasound observations highlighting enhanced detection capability for sources located downwind of the stations (Ceranna et al., 2018).

To evaluate the detection thresholds, we consider the constraints on the evaluation of the minimum measurable signal amplitude at the receivers. We adopt a statistical framework to develop a probabilistic measure of the minimum explosive yield detectable by the IMS infrasound network at any point on the globe. Here, the probabilistic method assumes that the model parameters cannot be accurately estimated. The model parameters describing the atmospheric structure, propagation characteristics, and recording conditions are drawn from normal distributions parameterized by a mean and a standard deviation.

3.2. Spectral Source Model

The spectral source model relates the estimated near-source characteristics of the acoustic signal to the explosive yield using established blast wave models. Semi-empirical models have been introduced to relate near-source spectral amplitude to yield (e.g., Kinney & Graham, 1985). An analytical form of the spectral amplitude (in dB, Pa/Hz) can be derived from an idealized blast-wave signal (Text S2 in Supporting Information S1)

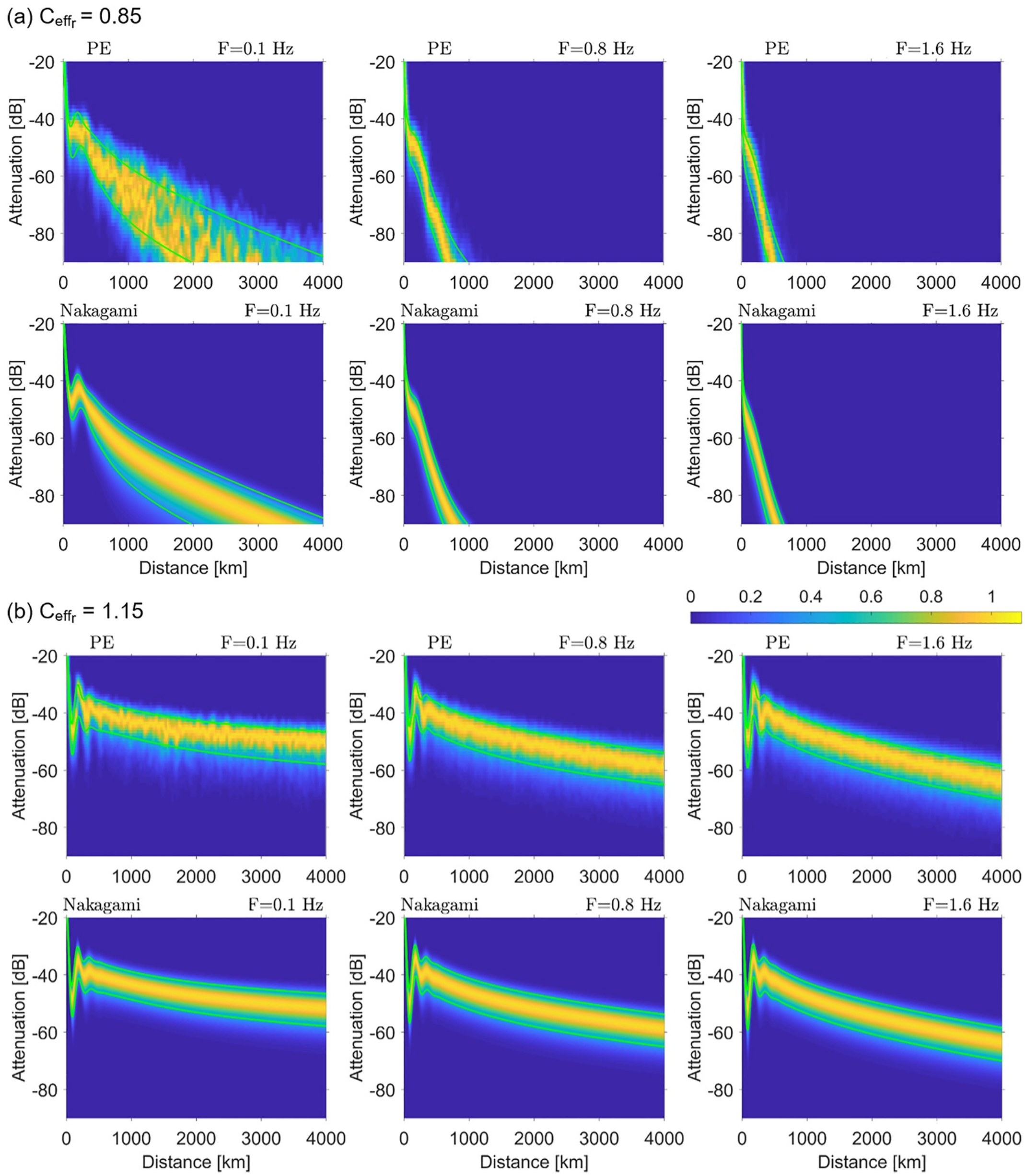

Figure 6. The top rows show the 2D-PE simulations results at 0.1 Hz (left column), 0.8 Hz (middle column) and 1.6 Hz (right column) for $C_{eff_r} = 0.85$ (a) and $C_{eff_r} = 1.15$ (b). The bottom rows show the corresponding Nakagami distribution probability (Nakagami, 1960), which fits the standard deviation (green lines) of the PE simulation results.

$$P_{dB}(W_J,f,r) = 20\log_{10}\left(p_0(W_J,r)\,t_0(W_J,r)\cdot\frac{2\pi f t_0(W_J,r)}{1+(2\pi f t_0(W_J,r))^2}\right), \tag{8}$$

where r is the propagation range (in meter), f is the frequency (in Hz), p_0 and t_0 are the peak overpressure and the positive phase duration of the blast wave respectively, and W_J is the explosive yield of the explosion (in Joule). The yield-doubling effect of near-surface explosions, as described by Kinney and Graham (1985), is here considered.

The expressions of p_0 and t_0 are introduced from the fits as follows (Korobeinikov, 1985)

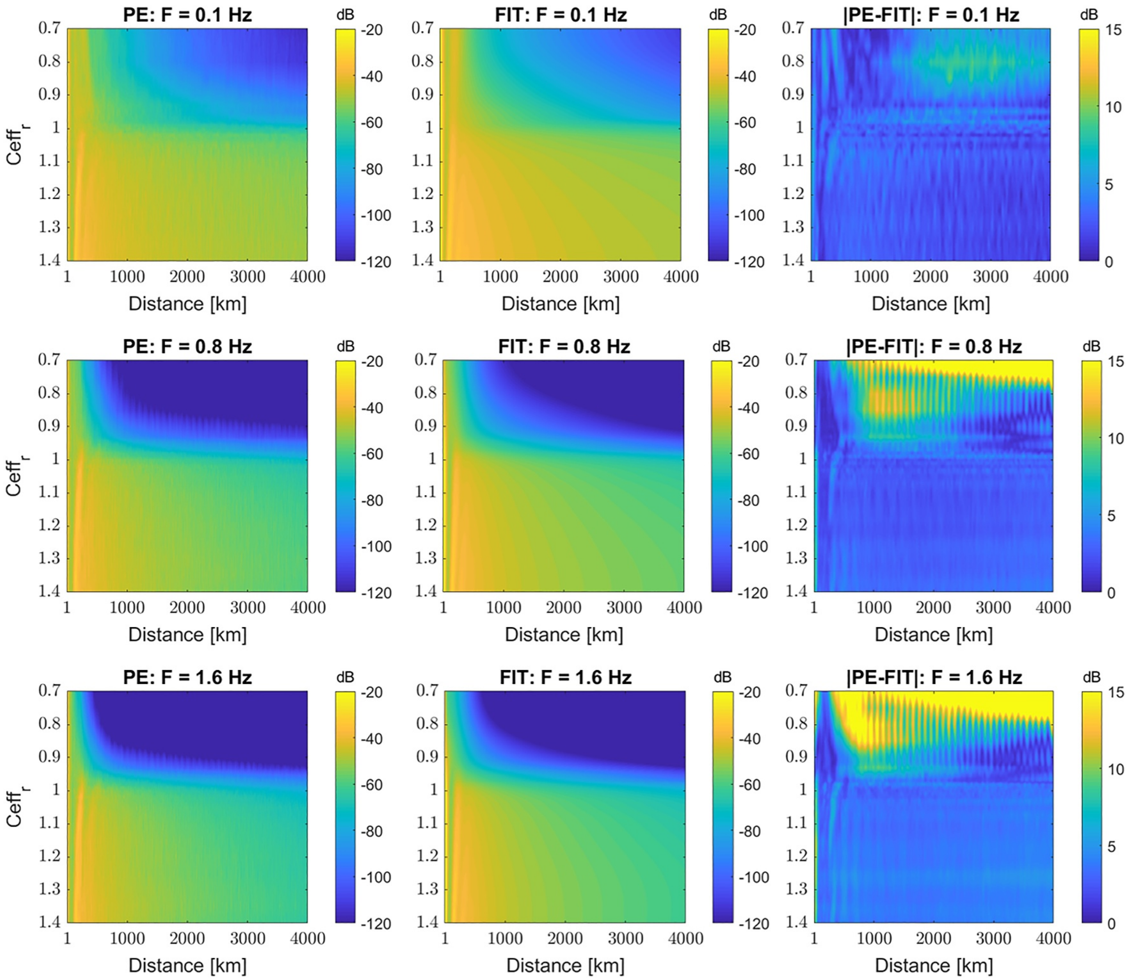

Figure 7. Comparison between 2D-PE simulations (left column) and curve fitting results (middle column) as a function of C_{eff_r} and propagation range, for a source frequency of 0.1 Hz (top row), 0.8 Hz (middle row), and 1.6 Hz (bottom row). Right panels show the absolute value of the difference between the simulations and curve fitting results (in dB). The color scale codes the pressure attenuation (in dB).

$$p_0 = \frac{0.326 P_0}{Z_j \cdot \sqrt{1 + \log\left(\frac{Z_j}{2}\right)}}, \tag{9}$$

$$t_0 = \frac{R_0}{c_0}\left(Z_j - 0.24 - \left(Z_j - 0.22\sqrt{\gamma} - \frac{0.4}{\sqrt{2\alpha\gamma}}\sqrt{1 + \log\left(\frac{Z_j}{2}\right)}\right)\right), \tag{10}$$

where P_0 is the atmospheric pressure, c_0 is the sound speed, $\gamma = 1.4$ is the ratio of specific heats, $\alpha = 0.805$, and R_0 is the charge equivalent radius of a point explosion given by

$$R_0 = \left(\frac{W_J}{P_0}\right)^{\frac{1}{3}}. \tag{11}$$

The quantity Z_j refers to the normalized distance

$$Z_j = \frac{r}{R_0}. \tag{12}$$

3.3. A Statistical Framework for the Yield Estimation

To quantify the detection capability, the transmission loss statistics derived from Equation 3 are combined with an analytic form of the spectral amplitude of the ground explosions and the spectral distribution of the background noise. The propagation-based probability distribution of the source spectral amplitude at the receiver is computed by combining the distribution of the logarithm of the near-source spectral amplitude (Equation 8) and transmission loss statistics.

Using Equation 4, the Nakagami-m distribution is represented as

$$\rho_{arr}(P_{dB}, W_J, f, R, C_{eff_r}) = \frac{2m^m}{20\log_{10}(e)\Gamma(m)} e^{\left[m\left(\frac{2(P_{dB}-\Omega_{dB})}{20\log_{10}(e)} - e^{\frac{2(P_{dB}-\Omega_{dB})}{20\log_{10}(e)}} \right) \right]}, \tag{13}$$

where P_{dB} is the spectral source model (in dB) defined by Equation 8, $\Omega_{dB} = 10\log_{10}(\Omega)$ (see Equations 5–7 for the expressions of Ω and m).

The probability that the noise at the station has a spectral amplitude less than or equal to that of the arrival signal is given by

$$\rho_{\det}(W_J, f, R, C_{eff_r}, N) = \int \rho_{arr}(P, W_J, f, R, C_{eff_r}) \cdot R_{ns}(P, f, R, N)\, dP, \tag{14}$$

where R_{ns} is the cumulative distribution of the effective noise statistics ρ_{ns} derived from Equation 1

$$R_{ns}(P, f, r, N) = \int_{-\infty}^{P} \rho_{ns}(P', f, r, N)\, dP'. \tag{15}$$

From Equation 14, we compute the 90% probability $\rho_{\det}$ for detecting an explosive yield W_J at a frequency f. The energy E_{eq} (in tons of TNT equivalent) is derived using $W_J = 4.184 \cdot 10^9 E_{eq}$.

4. Results

4.1. Validation Using Multi-Year Records of Volcanic Eruptions

Similar to previous validation studies (e.g., Antier et al., 2007; Le Pichon et al., 2021), we use multi-year infrasound detections of eruptive episodes at Mount Etna (37.73N, 15.00E, Sicily, Italy) recorded at the IMS station I48TN (35.80N, 9.32E, Tunisia), 550 km away from the volcano. In Europe, Mount Etna is the most active volcano, undergoing a variety of eruptive styles. Its volcanic activity is characterized by effusive eruptions from vents or fissures that produce voluminous lava flows, as well as sustained explosive activity, including Strombolian explosions, lava fountains, and sustained degassing (Marchetti et al., 2009). Due to its regular activity, Mount Etna is a unique source of repetitive signals that are valuable in providing constraints on the expected transmission loss (Assink et al., 2012). Its nearly continuous and high activity allows the study of stratospheric propagation along well-defined paths with time resolutions ranging from hours to several years.

Since July 2007, the University of Florence (UNIFI, Italy) has been operating a small-aperture (~250 m) array at an altitude of about 2,000 m. This array (ETN) is located southeast of the crater at a distance of 5 km from the main vents. ETN consists of four differential microbarometers with a flat frequency response in the 0.01–100 Hz band. The dynamic range of 200 Pa peak-to-peak allows monitoring signals from mild Strombolian explosions as well as major lava fountain events (Marchetti et al., 2018). For the purpose of this study, ETN records are processed in a single broad frequency band between 0.6 and 3 Hz. Detections related to volcanic activity are selected according to back-azimuths ranging between 300° and 360°. ETN detections are used to capture the source term (origin time, peak-to-peak amplitude, frequency at the maximum amplitude).

Figure 8a shows the 3-day median of peak-to-peak infrasonic amplitudes of volcanic activity between January 2019 and January 2022 (red dots). Infrasound data allow to follow the variable volcanic activity: from fairly stable activity throughout 2019, the signal amplitude peaked between May and July 2020 as a consequence of intense spattering and moderate Strombolian explosions from the summit craters. Signals were highly variable starting

10.1029/2025JD044937

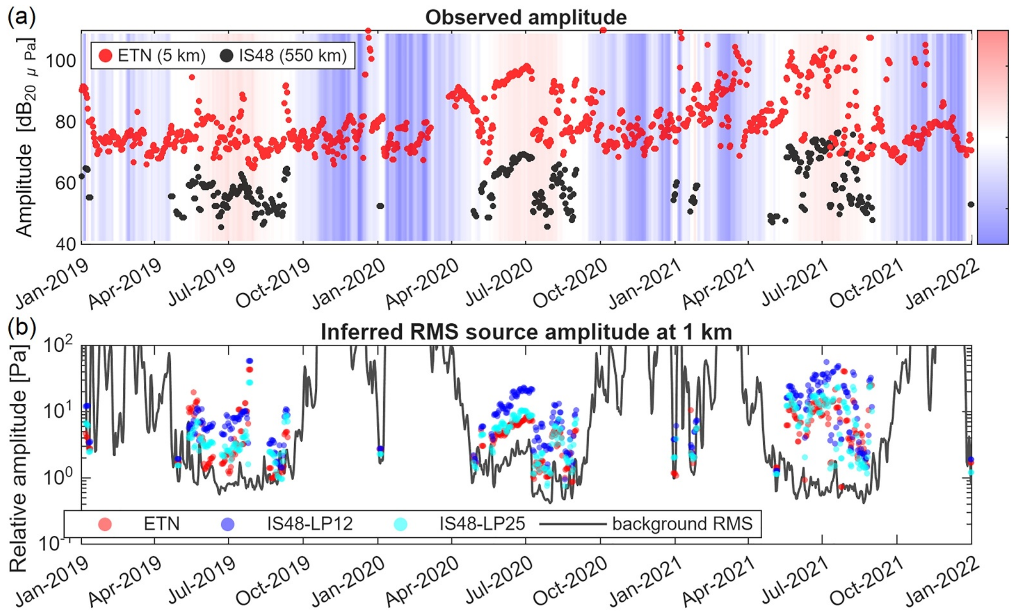

Figure 8. Comparison of near-field and far-field observations of eruptions at Mount Etna from 2019 to 2021. (a) Observed amplitudes at I48TN (at 550 km, black dots) and ETN array (at 5 km, red dots). I48TN mainly detects arrivals when C_{eff_r} (background color) is close to (white) or above one (reddish). All depicted amplitude values are the 3-day medians calculated using a sliding window at time steps of one-day. (b) Inferred (from I48TN data using LP12 in dark blue and LP25 in light blue) and observed (at ETN; in red) source amplitudes corrected for geometrical spreading to a reference distance of 1 km from the source. The background RMS amplitude (in the 0.64–2.56 Hz band; gray line) refers to the median of the hourly propagation-corrected (LP25) background noise at I48TN.

from February 2021, when a phase of repeating lava fountains started and persisted for several months (Moreno et al., 2024; Pardini et al., 2022; Proietti et al., 2023).

The Progressive Multi-Channel Correlation method (PMCC; Cansi, 1995) is applied to process the array records of I48TN. Frequency bands are scaled logarithmically using the one-third octave scheme between 0.1 and 5 Hz. The time windows are linearly scaled to the period with a 90% overlap. Such a setting is optimized to improve the array detection capability while allowing better discrimination between interfering signals over a wide frequency band (Hupe et al., 2022). The calculated wave parameters (e.g., back-azimuth and trace velocity) allow the identification of Etna-associated signals from the full detection list. We consider detections within the 0.6–3 Hz band, with trace velocities typical for stratospheric arrivals (330–380 m/s) and a back-azimuth range of ±10° around the true direction of Etna from I48TN (65.5°). To reduce false alarms, detections with peak-to-peak amplitudes larger than four times the standard deviation of a multi-year mean (2019–2021) are excluded. In addition, since signals from Mount Etna essentially propagate through the stratospheric waveguide (Assink, Le Pichon et al., 2014), detections corresponding to $C_{eff_r} < 1$ are discarded. The median frequency of the candidate detections at I48TN is 1.4 Hz (mostly confined between 0.91 and 1.76 Hz marking the 10th and 90th percentiles, respectively).

For the comparison of peak-to-peak amplitudes of the detections at I48TN and ETN, we identify detections at I48TN that correspond to at least one detection at ETN. More specifically, we apply the following criteria

$$t_{\mathrm{ETN}} + t_{\mathrm{prop\text{-}min}} \le t_{\mathrm{I48TN}} \le t_{\mathrm{ETN}} + t_{\mathrm{prop\text{-}max}}, \tag{16}$$

where t_{ETN} and t_{I48TN} are the detection times at ETN and I48TN respectively, and $t_{\mathrm{prop\text{-}min}}$ and $t_{\mathrm{prop\text{-}max}}$ are the minimum and maximum propagation times from ETN to I48TN, assuming a celerity range of 280 m s^{-1} to 320 m s^{-1} for stratospheric arrivals (e.g., Nippress et al., 2014).

Figure 8a compares the near-field and far-field observations of eruptions at Mount Etna from 2019 to 2021. ETN (red dots) naturally detects more signals from Mount Etna than I48TN (black dots). When observations from both

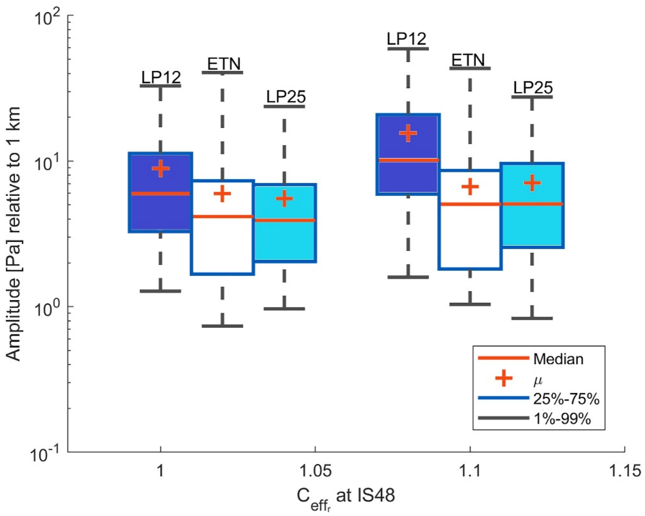

Figure 9. Whisker plots of the source amplitudes derived from LP12 (dark blue) and LP25 (light blue) attenuation relations, and observations at ETN (white). Statistics are grouped by effective sound speed ratios at the time of detection (from 1 to 1.04 on the left; from 1.05 to 1.14 on the right).

arrays are available, the variation of amplitudes qualitatively agrees well (e.g., consistent peaks in mid- 2019, 2020, and 2021). At I48TN (550 km from Mount Etna), signals are mostly detected from April to September, during the downwind season, when infrasound signals propagate through a well-established and stable westward stratospheric waveguide. The average transmission loss is around −50 dB (relative to a reference distance of 1 km). These values are in agreement with the theoretical estimates published by Assink, Le Pichon et al. (2014). Signals are also detected during anomalous winter time periods, including Sudden Stratospheric Warming (SSW) events (Charlton & Polvani, 2007). Previous studies have examined the effects of SSWs on infrasound propagation, such as the change in the direction of observed infrasound (Smets et al., 2016) and the bidirectional conditions of the middle atmospheric ducting (Assink, Waxler et al., 2014). The impact of polar vortex disruption on the detection capability at I48TN is illustrated by the SSW life cycles of 2019, 2020, and 2021. In particular, stratospheric wind reversals triggered by wavenumber 1 and 2 planetary waves explain the observed detection peaks in late December 2020 and mid-January 2021 (Rao et al., 2021).

Figure 8b compares the inferred source amplitude from I48TN observations using LP12 and LP25 attenuation relations to the measured amplitude at ETN (scaled to a reference distance of 1 km). The RMS noise amplitude of I48TN in the frequency band 0.64–2.56 Hz, centered near the dominant frequency range of Etna detections (1.6 Hz), is superimposed; this curve is corrected for attenuation and indicates the baseline detection threshold below which ETN detections are discarded. The median of the calculated source amplitudes is 4.1 Pa at I48TN (LP25) and 4.4 Pa at ETN. On an hourly basis, the LP25-predicted source amplitude agrees with the observations with an RMS error of 4.7 Pa (4.6 Pa in 2019, 1.3 Pa in 2020, 6.6 Pa in 2021). LP25 generally matches the observations better than LP12. Between May and July, LP12 overestimates transmission loss when C_{eff_r} exceeds 1.18 (Le Pichon et al., 2012). Therefore, the resulting source amplitudes are generally too high when stratospheric winds prevail. The largest discrepancies with LP12 are explained by C_{eff_r} values falling outside the domain used to construct the LP12 attenuation law (0.85–1.18).

Figure 9 summarizes the predicted and observed source amplitude as detailed in Figure 8. The resulting source amplitudes at 1 km from Mount Etna are shown for different values of C_{eff_r} (1 and 1.1), reflecting two different downwind propagation conditions toward I48TN. The LP25 attenuation relation yields more accurate estimates than LP12, which tends to overestimate the amplitudes. This is especially true when stratospheric ducting is well established ($C_{eff_r} = 1.1$) with a median value twice higher (10.1 Pa) compared to the LP25 median value (5.1 Pa).

4.2. Assessing the Detection Capability of the IMS Infrasound Network

To evaluate the performance of the IMS network, we consider the constraints on calculating the smallest detectable explosive yield by all individual stations. Simulations are carried out using 53 operating IMS stations. The spatial resolution of the global source grid is 0.5° in both latitude and longitude. For a given frequency and propagation range, the transmission loss along each source to receiver propagation path is computed using Equation 3. The effective sound speed ratio C_{eff_r} is averaged along the propagation path. The mean (μ_{TL}) and standard deviation (σ_{TL}) of the transmission loss are calculated using the tabulated values of the four parameters α, β, α_s, d_s and α_g (see Text S1 in Supporting Information S1).

The source frequency, which varies from 0.1 to 3.2 Hz with a one-third-octave band scaling, is used to compute the near-source spectral distribution, as described in Equation 8. From Equation 14, we derive the 90% probability that the noise at the station has a spectral amplitude less than or equal to that of the arrival signal for a given explosive yield (Blom et al., 2023). The explored yield range covers four orders of magnitude (100 values logarithmically spaced between 1 t and 10 kt). The probability distribution of the effective noise statistics ρ_{ns} (see Equation 15) is calculated using the hourly PSDs at each element of the array for a given propagation range and number of array elements (see Equation 1).

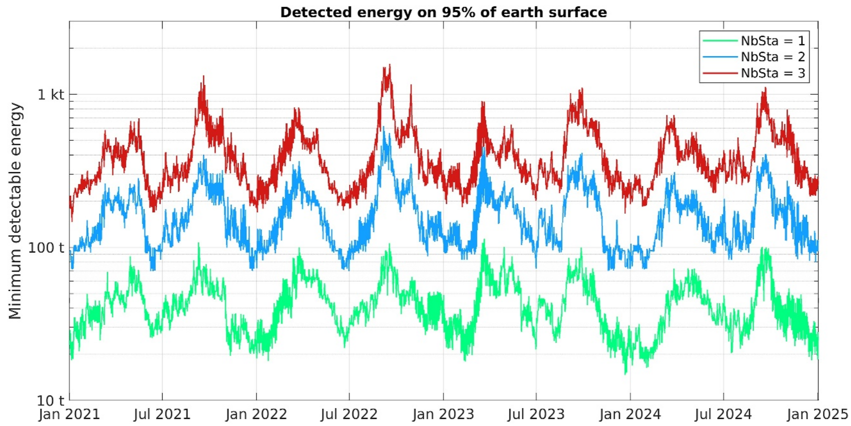

Figure 10. Temporal variation of the minimum detectable energy by 53 International Monitoring System stations on 95% of Earth's surface, distinguished by the number of detecting stations (*NbSta*) from January 2021 to January 2025 with a time resolution of 3 hr.

This statistical framework allows network performance predictions on a global scale with high temporal resolution (up to hourly scale). We investigate the effect of the number of detecting stations (*NbSta*) on the network performance. For each source grid, the smallest detectable explosive energy for all stations is sorted (from lowest to highest values). The detection threshold is then given by the ordinal rank assigned by *NbSta*. One-, two-, and three-station coverage correspond to an average inter-station spacing of 2,000, 2,290, and 2,520 km, respectively. Two-station coverage is the baseline condition to form an event. Compared with two-station coverage, three stations offer the advantage of reduced false alarms through redundant station detections, and improved location accuracy through reduction of sites aligned with the source.

Figure 10 shows multi-year fluctuations of the minimum detectable explosive energy. As expected, the network performance follows the general stratospheric wind circulation. The detection capability is enhanced in winter and summer when the prevailing stratospheric jet currents favor long-range propagation. During the transition between winter and summer, zonal winds reduce and reverse, yielding higher attenuation. The seasonal pattern is consistent with previous detection capability studies showing sinusoidal-like variation of the thresholds with improved detectability around January and July when the stratospheric winds are the strongest in both hemispheres (e.g., Green & Bowers, 2010). Near the equinox periods, from March to May and September to November, the stratospheric winds reduce, yielding an increase of the thresholds by a factor of ∼4. Overall, the detection capability with one-, two- and three-station coverage is ensured for explosive yield varying between ∼20–100 t, ∼70–500 t, and ∼200–1,300 t, respectively.

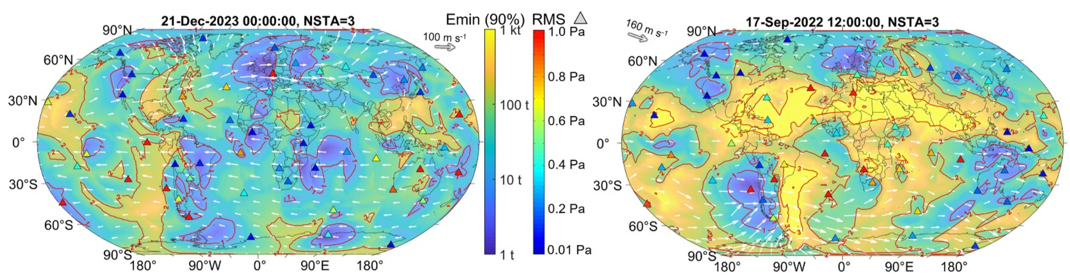

Figure 11. When requiring three detecting stations, the date with the lowest minimum detectable energy (95% of global coverage, 90% probability) and thus the best detection capability is 21 December 2023, 00:00 UTC (left panel). The date with the highest minimum detectable energy on global average is 17 September 2022, 12:00 UTC (right panel). White arrows depict the wind at ∼50 km altitude where the arrow size is scaled by the wind speed for each panel; the maxima are 100 m s^{-1} (left panel) and 160 m s^{-1} (right panel). The RMS colorbar depicts the noise level at the stations, derived from power spectral densities integration between 0.01 and 0.5 Hz (representing ambient noise including microbaroms). Red contour lines are labeled with the order of magnitude (1, 2, 3) for the yield in tons of TNT equivalent (10 t, 100 t, 1,000 t = 1 kt respectively).

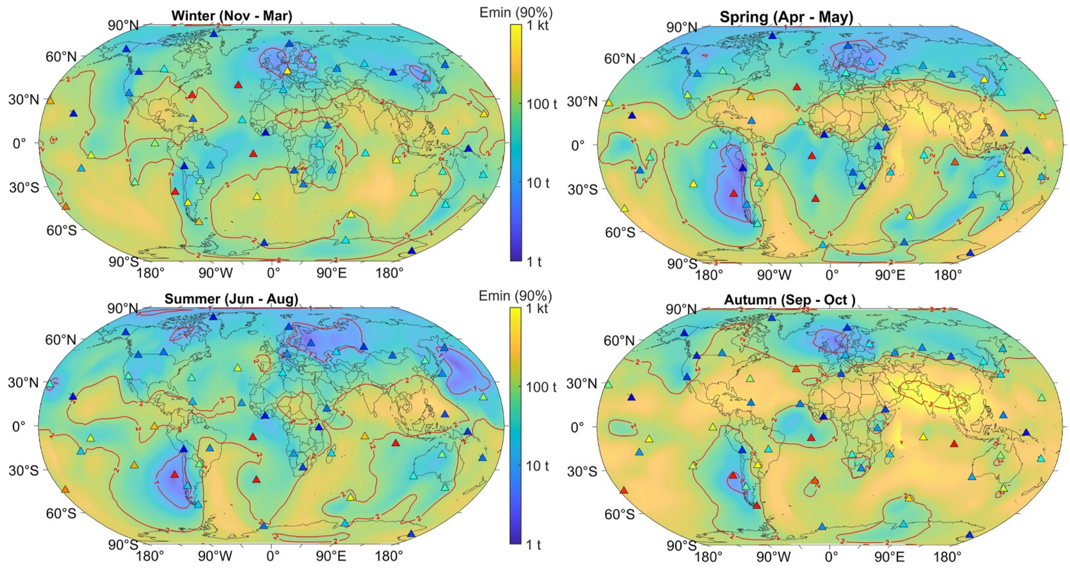

Figure 12. Comparison of the minimum detectable energy with three station coverage in winter, spring, summer, and autumn, averaged over four years (2021–2024). The colorbars and contour line labels are equivalent to those in Figure 11.

5. Discussion

Our simulations highlight the impact of the highly variable middle atmospheric dynamics and station noise levels on the detection capability. Figure 11 compares the geographical coverage of the globally lowest and highest minimum detectable energy with three station coverage, in the period depicted in Figure 10. The detection threshold varies from ∼200 t on 21 December 2023 to ∼1.3 kt on 17 September 2022.

Figure 12 shows how the geographical coverage of the minimum detectable energy attenuation varies by season. Improved performance is predicted during the solstice periods (January and July), when stratospheric winds are the strongest, compared to the equinox periods (April and October), when zonal winds reduce and reverse. These effects have already been highlighted by Le Pichon et al. (2009) and Green and Bowers (2010). The largest seasonal variations are observed in equatorial regions, where weak stratospheric winds produce an overall increase of the detection thresholds. Even under low stratospheric wind conditions, improved detection capability is predicted in mid-latitude regions of the Northern Hemisphere. The detection thresholds are generally larger (by one order of magnitude) across the oceans in all seasons due to the limited IMS network coverage and higher wind noise levels at island stations.

Figure 13 highlights regions where the temporal coverage required to guarantee 1 kt detection capability is less than 95%. These simulations indicate that the 1 kt design goal is not met in some regions as the IMS network is still under construction. In particular, in Southeast Asia, the temporal coverage for detecting 1 kt with three stations decreases down to 90%.

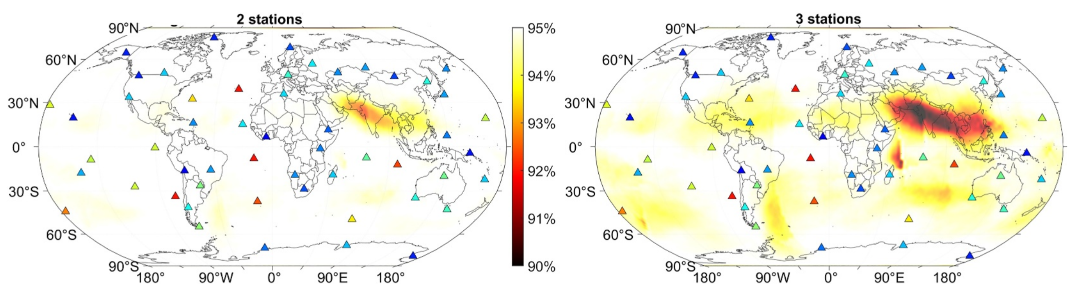

Figure 13. Percentage of time during which the minimum detectable energy by two stations (on the left) and three stations (on the right) is less than 1 kt of TNT over the 2021–2024 period. The colorbar for the station markers is equivalent to that in Figure 11.

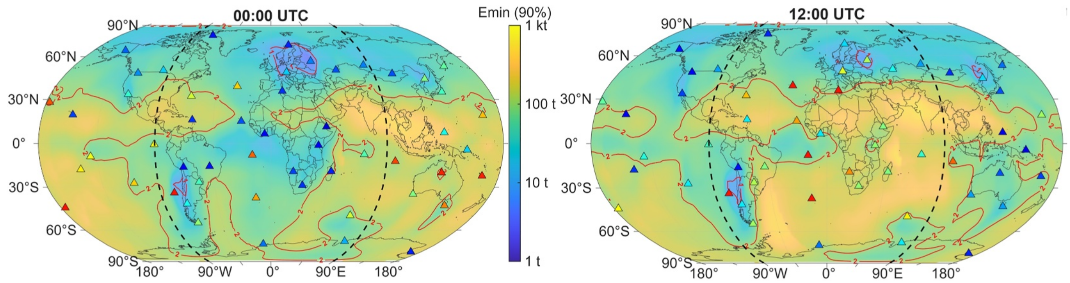

Figure 14. Comparison of the minimum detectable energy by three stations at 00:00 UTC (on the left) and 12:00 UTC (on the right), averaged over 4 years (2021–2024). The black dashed lines at 90W and 90E delimit the day and night time zones during the equinox periods. The colorbars and contour line labels are equivalent to those in Figure 11. See Figure S1 in Supporting Information S1 for the minimum detectable energy by two stations.

Figure 14 illustrates the impact of diurnal variations in station noise on the network performance. Comparing the detection capability maps at 0 UTC and 12 UTC shows improved performance at night (~20–200 t) on both sides of the meridian line and over the Pacific Ocean. During the day-time, the thresholds increase by up to one order of magnitude in the same regions. These predictions are consistent with the diurnal pattern of wind noise observed at most IMS stations (see Figure 5).

These simulations show that explosions equivalent to ~0.5 kt and ~1.3 kt would be detected at any time of the year by at least two and three stations, respectively. Indeed, in routine analysis, instrumental and environmental factors limit the detection capabilities. Aside from the SNR, which sets the threshold above which signals can be detected at the station, signals of interest must also be distinguishable from repetitive, coherent infrasonic signals. Moreover, hourly-calculated PSDs may not accurately reflect potential instrumental malfunctions. Thus, these thresholds should be considered optimistic detection limits.

Due to the high spatio-temporal variability of the winds in the ground-to-stratosphere levels, threshold variations reach one order of magnitude from seasonal down to semi-diurnal scales. Improved performance is predicted during the solstice periods when stratospheric winds are strongest. Around January and July, detection thresholds decrease down to ~70 t and ~200 t for two and three stations coverage, respectively. Furthermore, in the same regions, the thresholds increase by up to one order of magnitude from night- to daytime as a result of diurnal wind-noise pattern.

6. Conclusion

A new, physical-based attenuation relation (LP25) was derived from extensive 2D-PE simulations, employing archives of WACCM atmospheric specifications at all IMS stations. The relation incorporates the effects of the source frequency, the effective sound speed ratio in the stratosphere covering realistic down- and up-wind scenarios, and fine-scale atmospheric structures. The aim of these simulations is to increase understanding of the effect that these parameters have on long-range infrasound propagation. The LP25 attenuation relation quantifies attenuation in both the shadow zone and the geometrical acoustic duct region for stratospheric and thermospheric returns. Comparisons with multi-year records of Mount Etna activity in the near- and far field allow for a reliable statistical evaluation of the LP25 relation.

While previous studies have simplified the complexities of infrasound propagation and recording conditions, this study proposes a realistic statistical framework to quantify the 90% probability detection threshold of the IMS network for above-ground explosive events. The Nakagami-m distribution provides an accurate representation of the statistical distribution of reference transmission loss, with an average root mean square error of 5 dB. The resulting transmission loss model is used to estimate the spectral characteristics of explosive events near the source. To accurately describe station noise statistics, PSDs were computed using continuous historical records (2021–2024) from 53 certified IMS stations. These station-dependent noise models consider geographical and environmental parameters, revealing significant seasonal and diurnal variations. Using the tabulated attenuation relation parameters, detection thresholds can be calculated with limited computational resources and quantifiable uncertainties, making the framework suitable for operational monitoring purposes.

These simulations are in line with the results of earlier research (e.g., Green & Bowers, 2010; Le Pichon et al., 2009), despite the inherent complexities of the atmospheric structure being oversimplified. Our simulations show that near-surface atmospheric explosions with a minimum yield of ∼500 t of TNT equivalent can be detected by at least two stations at any time of year. They quantify the high variability of the detection thresholds with reliable uncertainty.

It is important to note that the propagation simulations were performed with the assumption of a source at ground-level. Based on the statistical approach we developed, the resulting attenuation remains valid for low-altitude explosions (e.g., up to a few kilometers), allowing for comparisons with both the LANL and AFTAC yield-period scaling relations. Herrin et al. (2008) present examples of explosions that occur at altitudes between 30 and 50 km, demonstrating the need for altitude corrections to accurately predict changes in signal frequency and amplitude. For high-altitude explosions, the decrease in atmospheric pressure and the increase in acoustic attenuation at the source location must be considered when predicting attenuation. As improving altitude corrections is outside the scope of this study, the results in this paper apply only to low-altitude explosions.

The statistical framework used here provides a basis for updating long-range propagation models. Assuming a stable effective sound speed profile and flat terrain can introduce errors when waves propagate over large distances. A more realistic picture of transmission loss statistics could be achieved by accounting for the variability of atmospheric specifications along propagation paths. Furthermore, constructing atmospheric state ensembles for each station and conducting 2D-PE simulations with terrain configuration are expected to reduce the variance in the predicted transmission losses.

Gardner's spectral model was used for its simplicity and tractability, but as a universal spectrum approach it does not account for geographical or temporal variability of GWs. This variability can impact how GWs combine with large-scale geometric wave guides to alter infrasound propagation across the IMS (Listowski et al., 2024). Moreover, the interaction of GWs with the mean flow is not represented in our approach. Therefore, the LP25 relation could benefit from recent 3D atmospheric models with higher vertical resolution extending to the upper atmosphere (e.g., Borchert et al., 2019). In particular, the Icosahedral Nonhydrostatic General Circulation Model (ICON) with an upper-atmospheric extension (UA-ICON) has benefited from recent developments in GW parameterizations that consider non-dissipative interactions between the mean and GW fields (Bölöni et al., 2021; Kim et al., 2021). Achieving more realistic MLT temperatures and zonal winds using the most applicable GW drag parameterization is still an active area of research (Kunze et al., 2025).

Similarly, the 2D-PE method used, with its known limitations (e.g., numerical sensitivity near turning points and near caustics that do not include out-of-plane scattering effects), may introduce biases in the simulations. More realistic results would be obtained through numerical exploration using fully resolved, time- and range-dependent wave propagation techniques that account for non-linear propagation and topography effects (Waxler & Assink, 2018). However, these numerical methods do not yet allow the exploration of a large parameter space for real-global and time operational applications. Metamodeling is a commonly used approach to simplify model representation and reduce computational burden. In this context, developing and comparing the performance of a cost-effective machine learning-based model against conventional numerical methods represents another challenge. Recent promising research exploiting deep learning approaches is capable of transmission loss predictions almost instantaneously in a range dependent atmosphere. Following the original convolutional neural network model developed by Brissaud et al. (2022), Cameijo et al. (2025) exploited convolutional recurrent architectures to capture both local and sequential atmospheric dynamics, allowing prediction of transmission losses over a distance of 4,000 km with a mean error of ∼5 dB. Such approaches mark a significant step toward near real-time evaluation of infrasound network detection thresholds. Compared to numerical wave propagation simulations, the gain in computation time is approximately four orders of magnitude.

Finally, further work is required to validate the calculated attenuation maps using ground-truth events. Efforts have been made to compile a comprehensive database of calibrated explosion experiments that can be used as ground truth. These databases are constantly updated and will provide a statistical approach for testing the attenuation model (Gibbons et al., 2018). Such repetitive sources provide opportunities to evaluate network performance simulation methods at a higher resolution.

Overall, these studies represent an important step toward establishing an effective monitoring regime for atmospheric events. In the context of the future verification of the CTBT, these simulations will be helpful in designing and prioritizing the maintenance of any infrasound monitoring network. Beyond the CTBT framework, developing an operational tool to optimize future network design and assess network performance in real-time promotes the potential benefits of infrasound technology for civil and scientific applications, such as regional and global volcanic activity monitoring (e.g., Gheri et al., 2023; Matoza et al., 2018).

Conflict of Interest

The authors declare no conflicts of interest relevant to this study.

Data Availability Statement

The command-line 2D-PE code is included in the NCPAprop modeling package provided by Waxler et al. (2021). WACCM data were obtained via the NCAR Research data archive (Atmospheric Chemistry Observations & Modeling, National Center for Atmospheric Research, University Corporation for Atmospheric Research, 2020). The DTK-GPMCC software included in the NDC-in-a-Box package designed for infrasound array processing is available upon request. Infrasound products derived from the comprehensive detection lists of the certified 53 IMS infrasound stations can be found at the BGR Geoportal (https://geoportal.bgr.de), see Hupe et al. (2022).

Acknowledgments
All authors thank the CTBTO and the IMS station operators for guaranteeing the high quality of the infrasound data and acknowledge the CTBTO Preparatory Commission for providing limited access (via vDEC) to the IMS infrasound network data. We would like to sincerely thank Philip S. Blom and two anonymous reviewers for their valuable feedback and constructive comments, which contributed to improving the quality of this paper.

References

Abbas, S., & Sheikh, A. (1996). A geometric theory of Nakagami fading multipath mobile radio channel with physical interpretations. *Proceedings of Vehicular Technology Conference VTC*, *2*, 637–641. https://doi.org/10.1109/VETEC.1996.501389

Antier, K., Le Pichon, A., Vergniolle, S., Zielinski, C., & Lardy, M. (2007). Multiyear validation of the NRL-G2S wind fields using infrasound from Yasur. *Journal of Geophysical Research*, *112*(D23), D23110. https://doi.org/10.1029/2007JD008462

Arrowsmith, S. J., & Hedlin, M. A. H. (2005). Observations of infrasound from surf in southern California. *Geophysical Research Letters*, *32*(9), L09810. https://doi.org/10.1029/2005GL022761

Assink, J. D., Le Pichon, A., Blanc, E., Kallel, M., & Khemiri, L. (2014). Evaluation of wind and temperature profiles from ECMWF analysis on two hemispheres using volcanic infrasound. *Journal of Geophysical Research: Atmospheres*, *119*(14), 8659–8683. https://doi.org/10.1002/2014JD021632

Assink, J. D., Waxler, R., & Drob, D. (2012). On the sensitivity of infrasonic traveltimes in the equatorial region to the atmospheric tides. *Journal of Geophysical Research*, *117*(D1), D01110. https://doi.org/10.1029/2011JD016107

Assink, J. D., Waxler, R., Frazier, W. G., & Lonzaga, J. (2013). The estimation of upper atmospheric wind model updates from infrasound data. *Journal of Geophysical Research: Atmospheres*, *118*(19), 10707–10724. https://doi.org/10.1002/jgrd.50833

Assink, J. D., Waxler, R., Smets, P., & Evers, L. G. (2014). Bidirectional infrasonic ducts associated with sudden stratospheric warming events. *Journal of Geophysical Research: Atmospheres*, *119*(3), 1140–1153. https://doi.org/10.1002/2013JD021062

Atmospheric Chemistry Observations & Modeling, National Center for Atmospheric Research, University Corporation for Atmospheric Research. (2020). *Whole atmosphere community climate model (WACCM) model output*. Research Data Archive at the National Center for Atmospheric Research, Computational and Information Systems Laboratory. Retrieved from https://rda.ucar.edu/datasets/d313006/

Blom, P. S., Dannemann, F. K., & Marcillo, O. E. (2018). Bayesian characterization of explosive sources using infrasonic signals. *Geophysical Journal International*, *215*(1), 240–251. https://doi.org/10.1093/gji/ggy258

Blom, P. S., Waxler, R., & Frazier, G. (2023). Quantification of spatial and seasonal trends in the atmosphere and construction of statistical models for infrasonic propagation. *Geophysical Journal International*, *235*(2), 1007–1020. https://doi.org/10.1093/gji/ggad260

Bölöni, G., Kim, Y.-H., Borchert, S., & Achatz, U. (2021). Toward transient subgrid-scale gravity wave representation in atmospheric models. Part I: Propagation model including nondissipative Wave–Mean-Flow interactions. *Journal of the Atmospheric Sciences*, *78*(4), 1317–1338. https://doi.org/10.1175/JAS-D-20-0065.1

Borchert, S., Zhou, G., Baldauf, M., Schmidt, H., Zängl, G., & Reinert, D. (2019). The upper-atmosphere extension of the icon general circulation model (version: Ua-icon-1.0). *Geoscientific Model Development*, *12*(8), 3541–3569. https://doi.org/10.5194/gmd-12-3541-2019

Bowman, J. R., Baker, G. E., & Bahavar, M. (2005). Ambient infrasound noise. *Geophysical Research Letters*, *32*(9), L09803. https://doi.org/10.1029/2005GL022486

Bowman, J. R., Shields, G., & O'Brien, M. S. (2009). Infrasound station ambient noise estimates and models: 2003–2006 (erratum). In *Infrasound technology workshop*.

Brachet, N., Brown, D., Le Bras, R., Cansi, Y., Mialle, P., & Coyne, J. (2009). Monitoring the Earth's atmosphere with the global IMS infrasound network. In A. Le Pichon, E. Blanc, & A. Hauchecorne (Eds.), *Infrasound monitoring for atmospheric studies* (pp. 77–118). Springer. https://doi.org/10.1007/978-1-4020-9508-5_3

Brissaud, Q., Näsholm, S. P., Turquet, A., & Le Pichon, A. (2022). Predicting infrasound transmission loss using deep learning. *Geophysical Journal International*, *232*(1), 274–286. https://doi.org/10.1093/gji/ggac307

Cameijo, A. J., Le Pichon, A., Sklab, Y., Arib, S., Brissaud, Q., Näsholm, S. P., et al. (2025). Toward real-time assessment of infrasound event detection capability using deep learning-based transmission loss estimation. *Journal of Geophysical Research: Atmospheres*, *130*(19). https://doi.org/10.1029/2025jd043577

Campus, P., & Christie, D. R. (2009). Worldwide observations of infrasonic waves. In A. Le Pichon, E. Blanc, & A. Hauchecorne (Eds.), *Infrasound monitoring for atmospheric studies* (pp. 185–234). Springer. https://doi.org/10.1007/978-1-4020-9508-5_6

Cansi, Y. (1995). An automatic seismic event processing for detection and location: The P.M.C.C. Method. *Geophysical Research Letters*, *22*(9), 1021–1024. https://doi.org/10.1029/95GL00468

Ceranna, L., Le Pichon, A., Green, D. N., & Mialle, P. (2009). The Buncefield explosion: A benchmark for infrasound analysis across Central Europe. *Geophysical Journal International*, *177*(2), 491–508. https://doi.org/10.1111/j.1365-246X.2008.03998.x

Ceranna, L., Matoza, R., Hupe, P., Le Pichon, A., & Landès, M. (2018). Systematic array processing of a decade of global IMS infrasound data. In A. Le Pichon, E. Blanc, & A. Hauchecorne (Eds.), *Infrasound monitoring for atmospheric studies: Challenges in middle atmosphere dynamics and societal benefits* (pp. 471–482). Springer. https://doi.org/10.1007/978-3-319-75140-5_13

Charlton, A. J., & Polvani, L. M. (2007). A new look at stratospheric sudden warmings. Part I: Climatology and modeling benchmarks. *Journal of Climate*, *20*(3), 449–469. https://doi.org/10.1175/JCLI3996.1

Che, I.-Y., Kim, I., Park, J., Kim, B.-I., & Kim, K. (2023). Detections of infrasound waves from water discharges at a hydroelectric dam: Implementation of timely warnings for unexpected discharge events. *Geophysical Research Letters*, *50*(10), e2023GL103026. https://doi.org/10.1029/2023GL103026

Christie, D. R., & Campus, P. (2009). The IMS infrasound network: Design and establishment of infrasound stations. In A. Le Pichon, E. Blanc, & A. Hauchecorne (Eds.), *Infrasound monitoring for atmospheric studies* (pp. 29–75). Springer. https://doi.org/10.1007/978-1-4020-9508-5_2

Chunchuzov, I. P., Kulichkov, S. N., Popov, O. E., Waxler, R., & Assink, J. (2011). Infrasound scattering from atmospheric anisotropic inhomogeneities. *Izvestiya Atmospheric and Oceanic Physics*, *47*(5), 540–557. https://doi.org/10.1134/s0001433811050045

Clauter, D. A., & Blandford, R. (1997). Capability modelling of the proposed international monitoring system 60-station infrasonic network. In *Proceedings of the infrasound workshop for CTBT monitoring, LA-UR-98-56*.

CTBTO. (2019). Operational manual for infrasound monitoring and the international exchange of infrasound data (CTBT/WGB/TL-11,17/17/Rev. 6) (p. 56).

Cugnet, D., de la Camara, A., Lott, F., Millet, C., & Ribstein, B. (2018). Non-orographic gravity waves: Representation in climate models and effects on infrasound. In A. Le Pichon, E. Blanc, & A. Hauchecorne (Eds.), *Infrasound monitoring for atmospheric studies: Challenges in middle atmosphere dynamics and societal benefits* (pp. 827–844). Springer. https://doi.org/10.1007/978-3-319-75140-5_27

De Carlo, M., Hupe, P., Le Pichon, A., Ceranna, L., & Ardhuin, F. (2021). Global microbarom patterns: A first confirmation of the theory for source and propagation. *Geophysical Research Letters*, *48*(3), e2020GL090163. https://doi.org/10.1029/2020GL090163

de Groot-Hedlin, C. D., & Hedlin, M. A. (2014). Infrasound detection of the Chelyabinsk meteor at the USArray. *Earth and Planetary Science Letters*, *402*, 337–345. https://doi.org/10.1016/j.epsl.2014.01.031

Drob, D. P. (2018). Explosion source models. In A. Le Pichon, E. Blanc, & A. Hauchecorne (Eds.), *Infrasound monitoring for atmospheric studies: Challenges in middle atmosphere dynamics and societal benefits* (pp. 485–508). Springer. https://doi.org/10.1007/978-3-319-75140-5_14

Drob, D. P., Broutman, D., Hedlin, M. A., Winslow, N. W., & Gibson, R. G. (2013). A method for specifying atmospheric gravity wavefields for long-range infrasound propagation calculations. *Journal of Geophysical Research: Atmospheres*, *118*(10), 3933–3943. https://doi.org/10.1029/2012JD018077

Drob, D. P., Emmert, J. T., Crowley, G., Picone, J. M., Shepherd, G. G., Skinner, W., et al. (2008). An empirical model of the Earth's horizontal wind fields: HWM07. *Journal of Geophysical Research*, *113*(A12), A12304. https://doi.org/10.1029/2008JA013668

Drob, D. P., Picone, J. M., & Garcés, M. (2003). Global morphology of infrasound propagation. *Journal of Geophysical Research*, *108*(D21), 4680. https://doi.org/10.1029/2002JD003307

Edwards, W. N., Brown, P. G., & ReVelle, D. O. (2006). Estimates of meteoroid kinetic energies from observations of infrasonic airwaves. *Journal of Atmospheric and Solar-Terrestrial Physics*, *68*(10), 1136–1160. https://doi.org/10.1016/j.jastp.2006.02.010

Farges, T., Hupe, P., Le Pichon, A., Ceranna, L., Listowski, C., & Diawara, A. (2021). Infrasound thunder detections across 15 years over Ivory Coast: Localization, propagation, and link with the stratospheric semi-annual oscillation. *Atmosphere*, *12*(9), 1188. https://doi.org/10.3390/atmos12091188

Fee, D., Waxler, R., Assink, J., Gitterman, Y., Given, J., Coyne, J., et al. (2013). Overview of the 2009 and 2011 Sayarim Infrasound Calibration Experiments. *Journal of Geophysical Research: Atmospheres*, *118*(12), 6122–6143. https://doi.org/10.1002/jgrd.50398

Garcés, M. (2018). Explosion source models. In A. Le Pichon, E. Blanc, & A. Hauchecorne (Eds.), *Infrasound monitoring for atmospheric studies: Challenges in middle atmosphere dynamics and societal benefits* (pp. 273–345). Springer. https://doi.org/10.1007/978-3-319-75140-5_8

Gardner, C. S., Hostetler, C. A., & Franke, S. J. (1993). Gravity wave models for the horizontal wave number spectra of atmospheric velocity and density fluctuations. *Journal of Geophysical Research*, *98*(D1), 1035–1049. https://doi.org/10.1029/92JD02051

Gasperini, F. (2019). *SD WACCM-X v2.1*. Research Data Archive at the National Center for Atmospheric Research, Computational and Information Systems Laboratory. Retrieved from https://rda.ucar.edu/datasets/d651034/

Gavin, H. P. (2013). The Levenberg-Marquardt method for nonlinear least squares curve-fitting problems c. Mathematics. Retrieved from https://api.semanticscholar.org/CorpusID:5708656

Gettelman, A., Mills, M. J., Kinnison, D. E., Garcia, R. R., Smith, A. K., Marsh, D. R., et al. (2019). The whole atmosphere community climate model version 6 (WACCM6). *Journal of Geophysical Research: Atmospheres*, *124*(23), 12380–12403. https://doi.org/10.1029/2019JD030943

Gheri, D., Marchetti, E., Belli, G., Le Pichon, A., Boulenger, V., Hupe, P., et al. (2023). Monitoring of Indonesian volcanoes with the IS06 infrasound array. *Journal of Volcanology and Geothermal Research*, *434*, 107753. https://doi.org/10.1016/j.jvolgeores.2023.107753

Gibbons, S., Kværna, T., & Näsholm, P. (2018). Characterization of the infrasonic wavefield from repeating seismo-acoustic events. In A. Le Pichon, E. Blanc, & A. Hauchecorne (Eds.), *Infrasound monitoring for atmospheric studies: Challenges in middle atmosphere dynamics and societal benefits* (pp. 387–407). Springer International Publishing. https://doi.org/10.1007/978-3-319-75140-5_10

Gómez-Déniz, E., & Gómez-Déniz, L. (2024). A new derivation of the Nakagami-m distribution as a composite of the Rayleigh distribution. *Wireless Networks*, *30*, 1–10. https://doi.org/10.1007/s11276-024-03713-5

Green, D. N., & Bowers, D. (2010). Estimating the detection capability of the International Monitoring System infrasound network. *Journal of Geophysical Research*, *115*(D18), D18116. https://doi.org/10.1029/2010JD014017

Green, D. N., & Nippress, A. (2019). Infrasound signal duration: The effects of propagation distance and waveguide structure. *Geophysical Journal International*, *216*(3), 1974–1988. https://doi.org/10.1093/gji/ggy530

Green, D. N., Vergoz, J., Gibson, R., Le Pichon, A., & Ceranna, L. (2011). Infrasound radiated by the Gerdec and Chelopechene explosions: Propagation along unexpected paths. *Geophysical Journal International*, *185*(2), 890–910. https://doi.org/10.1111/j.1365-246X.2011.04975.x

Hedlin, M. A. H., & Drob, D. P. (2014). Statistical characterization of atmospheric gravity waves by seismoacoustic observations. *Journal of Geophysical Research: Atmospheres*, *119*(9), 5345–5363. https://doi.org/10.1002/2013JD021304

Herrin, E. T., Bass, H. E., Andre, B., Woodward, R. L., Drob, D. P., Hedlin, M. A. H., et al. (2008). High-altitude infrasound calibration experiments. *Acoustics Today*, *4*(2), 9–21. https://doi.org/10.1121/1.2961169

Hupe, P., Ceranna, L., Le Pichon, A., Matoza, R. S., & Mialle, P. (2022). International monitoring system infrasound data products for atmospheric studies and civilian applications. *Earth System Science Data*, *14*(9), 4201–4230. https://doi.org/10.5194/essd-14-4201-2022

Hupe, P., Ceranna, L., Pilger, C., Le Pichon, A., Blanc, E., & Rapp, M. (2019). Mountain-associated waves and their relation to orographic gravity waves. *Meteorologische Zeitschrift*, *30*(1), 59–77. https://doi.org/10.1127/metz/2019/0982

Johnson, J. B. (2003). Generation and propagation of infrasonic airwaves from volcanic explosions. *Journal of Volcanology and Geothermal Research*, *121*(1), 1–14. https://doi.org/10.1016/S0377-0273(02)00408-0
Kim, J. Y., Kang, J.-S., & Joh, M. (2021). GPU acceleration of MPAS microphysics WSM6 using OpenACC directives: Performance and verification. *Computers & Geosciences*, *146*, 104627. https://doi.org/10.1016/j.cageo.2020.104627
Kinney, G. F., & Graham, K. J. (1985). *Explosive shocks in air*. Springer. https://doi.org/10.1007/978-3-642-86682-1
Korobeinikov, V. P. (1985). *Problems in the theory of point explosions*. Moscow Izdatel Nauka.
Kristoffersen, S. K., Le Pichon, A., Hupe, P., & Matoza, R. S. (2022). Updated global reference models of broadband coherent infrasound signals for atmospheric studies and civilian applications. *Earth and Space Science*, *9*(7), e2022EA002222. https://doi.org/10.1029/2022EA002222
Kulichkov, S. (2009). On the prospects for acoustic sounding of the fine structure of the middle atmosphere. In A. Le Pichon, E. Blanc, & A. Hauchecorne (Eds.), *Infrasound monitoring for atmospheric studies* (pp. 511–540). Springer Netherlands. https://doi.org/10.1007/978-1-4020-9508-5_16
Kunze, M., Zülicke, C., Siddiqui, T. A., Stephan, C. C., Yamazaki, Y., Stolle, C., et al. (2025). UA-ICON with the NWP physics package (version UA-ICON-2.1): Mean state and variability of the middle atmosphere. *Geoscientific Model Development*, *18*(11), 3359–3385. https://doi.org/10.5194/gmd-18-3359-2025
Le Pichon, A., Assink, J. D., Heinrich, P., Blanc, E., Charlton-Perez, A., Lee, C. F., et al. (2015). Comparison of co-located independent ground-based middle atmospheric wind and temperature measurements with numerical weather prediction models. *Journal of Geophysical Research: Atmospheres*, *120*(16), 8318–8331. https://doi.org/10.1002/2015JD023273
Le Pichon, A., Ceranna, L., & Vergoz, J. (2012). Incorporating numerical modeling into estimates of the detection capability of the IMS infrasound network. *Journal of Geophysical Research*, *117*(D5), 1025. https://doi.org/10.1029/2011JD016670
Le Pichon, A., Ceranna, L., Vergoz, J., & Tailpied, D. (2018). Modeling the detection capability of the global IMS infrasound network. In A. Le Pichon, E. Blanc, & A. Hauchecorne (Eds.), *Infrasound monitoring for atmospheric studies: Challenges in middle atmosphere dynamics and societal benefits* (pp. 593–604). Springer International Publishing. https://doi.org/10.1007/978-3-319-75140-5_17
Le Pichon, A., Maurer, V., Raymond, D., & Hyvernaud, O. (2004). Infrasound from ocean waves observed in Tahiti. *Geophysical Research Letters*, *31*, L19103. https://doi.org/10.1029/2004GL020676
Le Pichon, A., Pilger, C., Ceranna, L., Marchetti, E., Lacanna, G., Souty, V., et al. (2021). Using dense seismo-acoustic network to provide timely warning of the 2019 paroxysmal Stromboli eruptions. *Scientific Reports*, *11*, 14464. https://doi.org/10.1038/s41598-021-93942-x
Le Pichon, A., Vergoz, J., Blanc, E., Guilbert, J., Ceranna, L., Evers, L., & Brachet, N. (2009). Assessing the performance of the International Monitoring System's infrasound network: Geographical coverage and temporal variabilities. *Journal of Geophysical Research*, *114*(D8), D08112. https://doi.org/10.1029/2008JD010907
Letournel, P., Listowski, C., Bocquet, M., Le Pichon, A., & Farchi, A. (2024). Evaluating numerical weather prediction models in the middle atmosphere using coherent Oceanic acoustic noise observations. *Journal of Geophysical Research: Atmospheres*, *129*(23), e2024JD042034. https://doi.org/10.1029/2024JD042034
Listowski, C., Stephan, C. C., Le Pichon, A., Hauchecorne, A., Kim, Y.-H., Achatz, U., & Bölöni, G. (2024). Stratospheric gravity waves impact on infrasound transmission losses across the international monitoring system. *Pure and Applied Geophysics*. https://doi.org/10.1007/s00024-024-03467-3
Lott, F., & Millet, C. (2009). The representation of gravity waves in atmospheric general circulation models (GCMs). In A. Le Pichon, E. Blanc, & A. Hauchecorne (Eds.), *Infrasound monitoring for atmospheric studies* (pp. 685–699). Springer. https://doi.org/10.1007/978-1-4020-9508-5_23
Marchetti, E., Ripepe, M., Campus, P., Le Pichon, A., Brachet, N., Blanc, E., et al. (2018). Infrasound monitoring of volcanic eruptions and contribution of ARISE to the Volcanic Ash Advisory Centers. In A. Le Pichon, E. Blanc, & A. Hauchecorne (Eds.), *Infrasound monitoring for atmospheric studies: Challenges in middle atmosphere dynamics and societal benefits* (pp. 1141–1162). Springer. https://doi.org/10.1007/978-3-319-75140-5_36
Marchetti, E., Ripepe, M., Ulivieri, G., Caffo, S., & Privitera, E. (2009). Infrasonic evidences for branched conduit dynamics at Mt. Etna volcano, Italy. *Geophysical Research Letters*, *36*(19), L19308. https://doi.org/10.1029/2009GL040070
Marcillo, O., Arrowsmith, S., Whitaker, R., Anderson, D., Nippress, A., Green, D. N., & Drob, D. (2013). Using physics-based priors in a Bayesian algorithm to enhance infrasound source location. *Geophysical Journal International*, *196*(1), 375–385. https://doi.org/10.1093/gji/ggt353
Marty, J. (2018). The IMS infrasound network: Current status and technological developments. In A. Le Pichon, E. Blanc, & A. Hauchecorne (Eds.), *Infrasound monitoring for atmospheric studies: Challenges in middle atmosphere dynamics and societal benefits* (pp. 3–62). Springer. https://doi.org/10.1007/978-3-319-75140-5_1
Marty, J., Doury, B., & Kramer, A. (2021). Low and high broadband spectral models of atmospheric pressure fluctuation. *Journal of Atmospheric and Oceanic Technology*, *38*(10), 1813–1822. https://doi.org/10.1175/JTECH-D-21-0006.1
Matoza, R., Fee, D., Green, D., & Mialle, P. (2018). Volcano infrasound and the international monitoring system. In A. Le Pichon, E. Blanc, & A. Hauchecorne (Eds.), *Infrasound monitoring for atmospheric studies: Challenges in middle atmosphere dynamics and societal benefits* (pp. 1023–1077). Springer. https://doi.org/10.1007/978-3-319-75140-5_33
Mialle, P., Brown, D., & Arora, N. (2018). Advances in operational processing at the international data Centre. In A. Le Pichon, E. Blanc, & A. Hauchecorne (Eds.), *Infrasound monitoring for atmospheric studies: Challenges in middle atmosphere dynamics and societal benefits* (pp. 209–248). Springer. https://doi.org/10.1007/978-3-319-75140-5_6
Moré, J. J. (1978). The Levenberg-Marquardt algorithm: Implementation and theory. In G. A. Watson (Ed.), *Numerical analysis* (pp. 105–116). Springer. https://doi.org/10.1007/BFb0067700
Moreno, J. M., Cannata, A., Di Grazia, G., Sciotto, M., & Soñora, J. P. (2024). Investigating Mt. Etna lava fountains by seismic and infrasonic signals: 14-21 February 2021 case study. *Annals of Geophysics*, *67*(2), VO217. https://doi.org/10.4401/ag-9053
Morton, E. A., & Arrowsmith, S. J. (2014). The development of global probabilistic propagation look-up tables for infrasound celerity and back-azimuth deviation. *Seismological Research Letters*, *85*(6), 1223–1233. https://doi.org/10.1785/0220140124
Mykkeltveit, S., Åstebøl, K., Doornbos, D. J., & Husebye, E. S. (1983). Seismic array configuration optimization. *Bulletin of the Seismological Society of America*, *73*(1), 173–186. https://doi.org/10.1785/BSSA0730010173
Nakagami, M. (1960). The m-distribution—A general formula of intensity distribution of rapid fading. In W. Hoffman (Ed.), *Statistical methods in radio wave propagation* (pp. 3–36). Pergamon. https://doi.org/10.1016/B978-0-08-009306-2.50005-4
Nippress, A., Green, D. N., Marcillo, O. E., & Arrowsmith, S. J. (2014). Generating regional infrasound celerity-range models using ground-truth information and the implications for event location. *Geophysical Journal International*, *197*(2), 1154–1165. https://doi.org/10.1093/gji/ggu049

Pardini, F., de'Michieli Vitturi, M., Andronico, D., Esposti Ongaro, T., Cristaldi, A., & Neri, A. (2022). Real-time probabilistic assessment of volcanic hazard for tephra dispersal and fallout at Mt. Etna: The 2021 lava fountain episodes. *Bulletin of Volcanology*, *85*(1), 6. https://doi.org/10.1007/s00445-022-01614-z

Pasolini, C. (2008). *The attenuation of seismic intensity (doctoral dissertation)*. Alma Mater Studiorum Università di Bologna. https://doi.org/10.6092/unibo/amsdottorato/868

Picone, J., Hedin, A., Drob, D., Meier, R., Lean, J., Nicholas, A., & Thonnard, S. (2000). Enhanced empirical models of the thermosphere. *Physics and Chemistry of the Earth - Part C: Solar, Terrestrial & Planetary Science*, *25*(5), 537–542. https://doi.org/10.1016/S1464-1917(00)00072-6

Proietti, C., De Beni, E., Cantarero, M., Ricci, T., & Ganci, G. (2023). Rapid provision of maps and volcanological parameters: Quantification of the 2021 Etna volcano lava flows through the integration of multiple remote sensing techniques. *Bulletin of Volcanology*, *85*(10), 58. https://doi.org/10.1007/s00445-023-01673-w

Rao, J., Garfinkel, C. I., Wu, T., Lu, Y., Lu, Q., & Liang, Z. (2021). The January 2021 sudden stratospheric warming and its prediction in subseasonal to seasonal models. *Journal of Geophysical Research: Atmospheres*, *126*(21), e2021JD035057. https://doi.org/10.1029/2021JD035057

Raspet, R., & Webster, J. (2013). Wind noise under a pine tree canopy. *Journal of the Acoustical Society of America*, *137*(2), 651–659. https://doi.org/10.1121/1.4906587

Rienecker, M. M., Suarez, M., Todling, R., Backmeister, J., Takacs, L., Liu, H.-C., et al. (2008). The GEOS-5 Data Assimilation System: Documentation of Versions 5.0 and 5.1. In *Technical report, NASA/TM-2008-104606* (p. 27). Retrieved from https://ntrs.nasa.gov/

Smets, P. S. M., Assink, J. D., Le Pichon, A., & Evers, L. G. (2016). ECMWF SSW forecast evaluation using infrasound. *Journal of Geophysical Research: Atmospheres*, *121*(9), 4637–4650. https://doi.org/10.1002/2015JD024251

Stevens, J. L., Divnov, I. I., Adams, D. A., Murphy, J. R., & Bourchik, V. N. (2002). Constraints on infrasound scaling and attenuation relations from soviet explosion data. In Z. A. Der, R. H. Shumway, & E. T. Herrin (Eds.), *Monitoring the comprehensive nuclear-test-ban treaty: Data processing and infrasound*. Birkhäuser Basel. https://doi.org/10.1007/978-3-0348-8144-9_8

Sutherland, L. C., & Bass, H. E. (2004). Atmospheric absorption in the atmosphere up to 160 km. *Journal of the Acoustical Society of America*, *115*(3), 1012–1032. https://doi.org/10.1121/1.1631937

Tsui, P.-H., Ho, M.-C., Tai, D.-I., Lin, Y.-H., Wang, C.-Y., & Ma, H.-Y. (2016). Acoustic structure quantification by using ultrasound Nakagami imaging for assessing liver fibrosis. *Scientific Reports*, *6*(1), 33075. https://doi.org/10.1038/srep33075

Vorobeva, E., Assink, J., Espy, P. J., Renkwitz, T., Chunchuzov, I., & Näsholm, S. P. (2023). Probing gravity waves in the middle atmosphere using infrasound from explosions. *Journal of Geophysical Research: Atmospheres*, *128*(13), e2023JD038725. https://doi.org/10.1029/2023JD038725

Walker, K. T., & Hedlin, M. A. (2009). A review of wind-noise reduction methodologies. In A. Le Pichon, E. Blanc, & A. Hauchecorne (Eds.), *Infrasound monitoring for atmospheric studies* (pp. 141–182). Springer Netherlands. https://doi.org/10.1007/978-1-4020-9508-5_5

Walker, K. T., Le Pichon, A., Kim, T. S., de Groot-Hedlin, C., Che, I.-Y., & Garcés, M. (2013). An analysis of ground shaking and transmission loss from infrasound generated by the 2011 Tohoku earthquake. *Journal of Geophysical Research: Atmospheres*, *118*(23), 12-831. https://doi.org/10.1002/2013JD020187

Waxler, R., & Assink, J. (2018). Propagation modeling through realistic atmosphere and benchmarking. In A. Le Pichon, E. Blanc, & A. Hauchecorne (Eds.), *Infrasound monitoring for atmospheric studies: Challenges in middle atmosphere dynamics and societal benefits* (pp. 509–549). Springer. https://doi.org/10.1007/978-3-319-75140-5_15

Waxler, R., Hetzer, C., & Assink, J. (2021). chetzer-ncpa/ncpaprop-release: Ncpaprop v2.1.0 [Software]. *Zenodo*. https://doi.org/10.5281/zenodo.5562713

Welch, P. (1967). The use of fast Fourier transform for the estimation of power spectra: A method based on time averaging over short, modified periodograms. *IEEE Transactions on Audio and Electroacoustics*, *15*(2), 70–73. https://doi.org/10.1109/TAU.1967.1161901

Whitaker, R. W. (1997). Infrasonic monitoring. In *17th annual seismic research symposium*.

Whitaker, R. W., Sandoval, T. D., & Mutschlecner, J. P. (2003). Recent infrasound analysis. In *25th annual seismic research symposium*.

Zhang, S., Zhou, F., Wan, M., Wei, M., Fu, Q., Wang, X., & Wang, S. (2012). Feasibility of using Nakagami distribution in evaluating the formation of ultrasound-induced thermal lesions. *Journal of the Acoustical Society of America*, *131*(6), 4836–4844. https://doi.org/10.1121/1.4711005

References From the Supporting Information

Friedlander, F. G. (1946). The diffraction of sound pulses, I. Diffraction by a semi-infinite plane. *The Royal Society*, *186*(1006), 322–344. https://doi.org/10.1098/rspa.1946.0046